

1  
2  
3  
4  
5  
6  
7  
8  
9  
10  
11  
12  
13  
14  
15  
16  
17  
18  
19  
20  
21  
22  
23  
24  
25  
26  
27  
28  
29  
30  
31  
32  
33

**Leader  $\beta$  cells coordinate  $\text{Ca}^{2+}$  dynamics across pancreatic islets**  
***in vivo***

Victoria Salem<sup>1,†</sup>, Luis Delgadillo Silva<sup>2†</sup>, Kinga Suba<sup>1</sup>, Eleni Georgiadou<sup>1</sup>, S. Neda Mousavy Gharavy<sup>1</sup>, Nadeem Akhtar<sup>2</sup>, Aldara Martin-Alonso<sup>1</sup>, David C.A. Gaboriau<sup>4</sup>, Stephen M. Rothery<sup>4</sup>, Theodoros Stylianides<sup>3</sup>, Gaëlle Carrat<sup>1</sup>, Timothy J. Pullen<sup>5</sup>, Sumeet Pal Singh<sup>2</sup>, David J. Hodson<sup>6,7</sup>, Isabelle Leclerc<sup>1</sup>, A.M. James Shapiro<sup>8</sup>, Piero Marchetti<sup>9</sup>, Linford J.B. Briant<sup>10</sup>, Walter Distaso<sup>11</sup>, Nikolay Ninov<sup>2,12\*</sup> and Guy A. Rutter<sup>1\*</sup>

<sup>1</sup>Department of Medicine, Imperial College London, London, UK, <sup>2</sup>DFG-Center for Regenerative Therapies, Technische Universität Dresden, Dresden, Germany, <sup>3</sup>Loughborough University, Loughborough, UK, <sup>4</sup>FILM, Imperial College London, London, UK, <sup>5</sup>Department of Diabetes, Faculty of Life Science and Medicine, King's College London, London, UK, <sup>6</sup>Institute of Metabolism and Systems Research (IMSR), University of Birmingham, Edgbaston, UK, <sup>7</sup>Centre for Endocrinology, Diabetes and Metabolism, Birmingham Health Partners, Birmingham, UK; and COMPARE University of Birmingham and University of Nottingham Midlands, <sup>8</sup> Clinical Islet Laboratory and Clinical Islet Transplant Program, University of Alberta, Edmonton, Alberta, Canada, <sup>9</sup>University of Pisa, Pisa, Italy, <sup>10</sup>Radcliffe Department of Medicine, University of Oxford, Oxford, UK. <sup>11</sup>Imperial College London, UK, <sup>12</sup>Paul Langerhans Institute Dresden of the Helmholtz Center Munich at the University Hospital Carl Gustav Carus of TU Dresden, German Center for Diabetes Research.

<sup>†</sup>Equal contributions

\*Corresponding authors: [g.rutter@imperial.ac.uk](mailto:g.rutter@imperial.ac.uk); [v.salem@imperial.ac.uk](mailto:v.salem@imperial.ac.uk); [nikolay.ninov@tu-dresden.de](mailto:nikolay.ninov@tu-dresden.de)

34 **ABSTRACT**

35

36 Pancreatic  $\beta$  cells form highly connected networks within isolated islets. Whether this  
37 behaviour pertains *in vivo*, after innervation and during continuous perfusion with blood, is  
38 unclear. Here, we use the recombinant  $\text{Ca}^{2+}$  sensor GCaMP6 to assess glucose-regulated  
39 connectivity in living zebrafish *D. rerio*, and in murine or human islets transplanted into the  
40 anterior eye chamber. In each setting,  $\text{Ca}^{2+}$  waves emanated from temporally-defined leader  
41  $\beta$  cells and 3D connectivity across the islet increased with glucose stimulation. Photo-  
42 ablation of zebrafish leader cells disrupted pan-islet signalling, identifying these as likely  
43 pacemakers. Correspondingly, in engrafted mouse islets, connectivity was sustained during  
44 prolonged glucose exposure, and super-connected “hub” cells were identified. Granger  
45 causality analysis revealed a controlling role for temporally-defined leaders, and  
46 transcriptomic analyses a discrete hub cell fingerprint. We thus define a population of  
47 regulatory  $\beta$  cells within coordinated islet networks *in vivo*. This population may drive  $\text{Ca}^{2+}$   
48 dynamics and pulsatile insulin secretion.

49

50 **WORDS: 150**

51

52 **Keywords:** Pancreatic islet, zebrafish, functional imaging,  $\text{Ca}^{2+}$  dynamics, GCaMP6,  $\beta$  cell,  
53 *in vivo*, connectivity, photo-ablation, transcriptomics, cluster analysis, Granger causality.

54 **INTRODUCTION.**

55

56 Defective insulin secretion underlies diabetes mellitus, a disease affecting almost 1 in 8 of  
57 the adult population worldwide, consuming 10 % of healthcare budgets of westernized  
58 societies (<https://www.idf.org/>). Impaired secretion is absolute in type 1 diabetes and relative  
59 in type 2 diabetes <sup>1</sup>.

60

61 Individual  $\beta$  cells within the pancreatic islets possess all of the enzymatic machinery required  
62 for glucose sensing and insulin secretion <sup>2, 3</sup>, although marked heterogeneity exists at the  
63 transcriptomic <sup>4, 5, 6, 7</sup>, metabolic <sup>8</sup>, electrophysiological <sup>9, 10</sup> and secretory <sup>11-13</sup> levels.  
64 Questions remain over whether this heterogeneity has any functional significance, and  
65 could, for example, contribute to the pulsatile release of insulin <sup>14</sup>.

66 Connections between individual  $\beta$  cells <sup>15, 16</sup> are essential for the normal control of hormone  
67 secretion <sup>10, 14, 17</sup>. Using  $\text{Ca}^{2+}$  imaging of isolated islets *in vitro* two distinct, but  
68 complementary, ways of analysing  $\beta$  cell connectivity have emerged. Earlier studies  
69 described an increase in the number of correlated cell pairs using Pearson-based analysis,  
70 which assesses similarities between the  $\text{Ca}^{2+}$  traces for individual cells over time <sup>18, 19</sup>. This  
71 strategy revealed that stimulation with glucose or glucagon like peptide-1 causes pan-islet  
72 increases in  $\beta$  cell connectivity which are disrupted under conditions mimicking type 2  
73 diabetes (e.g. “gluco(lipo)toxicity”). More recently, we have applied an approach based on  
74 signal binarization <sup>20</sup> and reported that a subset of 5-8 %  $\beta$  cells form super-connected  
75 “hubs” within the interconnected network <sup>18</sup>. We also demonstrated that these cells are likely  
76 to serve as pacemakers <sup>21</sup>. Both of these approaches utilise the term “connectivity” to  
77 describe the functional coactivity of  $\beta$  cells within an islet.

78 The behaviour of the isolated islet in culture <sup>18, 21</sup> is likely to differ significantly from that *in*  
79 *vivo* where islets are continuously perfused with blood and receive complex neural inputs.  
80 Imaging of the islet within the intact pancreas *in vivo* is, however, challenging and requires  
81 exteriorisation of the whole organ. A powerful alternative approach is the engraftment of  
82 islets into the anterior eye chamber <sup>22</sup>. Combined with the use of stably-expressed,  
83 recombinant fluorescent probes <sup>23, 24</sup> this creates an optically-accessible platform allowing  
84 repeated measurements over time if required <sup>25</sup>. Here, we use this strategy, alongside an  
85 analogous genetic modification of the zebrafish <sup>26</sup> to record multilayer  $\beta$  cell  $\text{Ca}^{2+}$  dynamics  
86 in the intact living animal <sup>27</sup>. Pancreatic islets display a largely conserved size, but partly  
87 species-specific <sup>28</sup> arrangement of neuroendocrine cell types <sup>29</sup>, important for the proper  
88 control of insulin secretion <sup>17</sup>. In the zebrafish, most of the pancreatic endocrine cells are  
89 located in a single primary islet <sup>27</sup>. By 5 days post fertilization (dpf) (as used in these

90 experiments) zebrafish larvae have developed a primary islet which contains an average of  
91 30  $\beta$  cells that express mature markers like Ucn3l<sup>26</sup>. Later in the juvenile stage, the  
92 zebrafish still possesses the large, embryonically-derived primary islet and has also  
93 developed many smaller secondary islets<sup>30</sup>. We have previously shown that the primary  
94 zebrafish islet responds *in vitro* to glucose<sup>26</sup> and ablation of  $\beta$  cells at this developmental  
95 stage leads to glucose intolerance in the larva<sup>31</sup>. Thus, by 5 dpf the primary islet is glucose  
96 responsive and systemically connected, serving as an excellent model to study islet  $\beta$  cell  
97 coordination.

98

99 We demonstrate that glucose induces strongly co-ordinated pan-islet  $\text{Ca}^{2+}$  responses in  
100 each setting, with a definable point of origin and propagation characteristics in three  
101 dimensions. In zebrafish, the ablation of “leader” cells, i.e. those which respond first to  
102 glucose challenge, results in a dampening of the response of the islet to subsequent  
103 stimulation with glucose, redolent to the effects of optogenetic inactivation of “hub” cells in  
104 the isolated mouse islet<sup>21</sup>. In the mouse, analyses based on signal binarization and Monte  
105 Carlo-like shuffling/randomisation<sup>21</sup> demonstrate the existence of a population of super-  
106 connected cells under stimulatory conditions *in vivo*. Moreover, causality analysis<sup>32, 33</sup> unites  
107 these observations in fish and mouse by demonstrating that temporally-defined “leader cells”  
108 are also those that were causally the most closely linked to other  $\beta$  cells, whilst analyses of  
109 single cell RNASeq data suggests they may possess a unique transcriptional profile. Hence,  
110 we demonstrate that a functional  $\beta$  cell hierarchy exists *in vivo*, and may control pulsatile  
111 insulin secretion.

112

113

114 **METHODS**

115

116 *Zebrafish husbandry.*

117 Zebrafish wild type (WT) AB, WIK and TL were used in all the experiments. Zebrafish were  
118 raised in standard conditions at 28 °C. Established transgenic lines used in this study were  
119 *Tg(ins:gCaMP6s;cryaa:mCherry)*<sup>26</sup>, *Tg(ins:cdt1-mCherry;cryaa:GFP)*<sup>31</sup> and  
120 *Tg(gata1a:DsRed)*<sup>26</sup>. *Tg(ins:cdt1-mCherry)* was utilised in preference of a pan  $\beta$  cell marker  
121 such as *Tg(ins:mKO-nls)* to allow for a clear separation of the spectra and simultaneous  
122 signal recordings from the GCaMP and mCherry channels, which was particularly important  
123 during fast imaging. All experiments were carried out in compliance with European Union  
124 and German laws (Tierschutzgesetz) and with the approval of the TU Dresden and the  
125 Landesdirektion Sachsen Ethics Committees (approval number: AZ 24D-9168,11-1/2013-14,  
126 TV38/2015, T12/2016, and T13/2016, TVV50/2017, and TVV 45/2018)). All live imaging *in*  
127 *vivo*, compound and glucose-injections, as well as experimental procedures were performed  
128 with zebrafish larvae that did not exceed five days post fertilization (dpf), as stated in the  
129 animal protection law (TierSchVersV §14). *Ex vivo* live-imaging of beta-cells was performed  
130 with isolated islets from euthanized fish according to approval T12/2016.

131

132 *Zebrafish glucose measurements.*

133 Groups of ten larvae were pooled together, snap frozen in liquid nitrogen, and then stored at  
134 -80°C. Following thawing on ice, 250  $\mu$ L of PBS were added and the larvae were sonicated  
135 with an ultrasonic homogenizer (Bandelin, SONOPLUS), prior to centrifugation at 13,000g.  
136 Glucose concentration was determined using the BioVision Glucose Assay Kit (Biovision Inc,  
137 California, US) according to the manufacturer's instructions.

138

139 *Intra-cardiac injection in zebrafish.*

140 Injections were performed using pulled glass pipettes with a 5nL tip volume calibrated  
141 microscopically (3.5" Drummond #3-000-203-G/X, Sutter pipette puller P-1000). A  
142 pneumatic pico-pump (FemtoJet, Eppendorf), injecting pressure 500 hPa and compensation  
143 pressure of 0 hPa, was used to deliver a 1 second injection into the pericardial cavity in the  
144 agarose-mounted larva, assisted by a micromanipulator (InjectMan N2, Eppendorf). Doses  
145 were 5 nL of 25 mM glucose and 5 nL insulin at 100 units/ml.

146

147 *Zebrafish live imaging.*

148 Embryos were treated with 0.003% (200  $\mu$ M) 1-phenyl 2-thiourea (PTU) to inhibit  
149 pigmentation from 1 dpf onwards. At 4.5 dpf, the larvae were anaesthetized using 0.4g/L

150 Tricaine. The larvae were mounted in glass-bottomed microwell dishes (MatTek corporation)  
151 using 1% low-melting agarose containing 0.4g/L Tricaine. After the agarose was solidified,  
152 the dishes were filled with embryonic fish water and 0.4g/L Tricaine. Live imaging was  
153 performed on an inverted laser scanning confocal system ZEISS LSM 780 inverted with a C-  
154 Apochromat 40X/N.A. 1.2 water correction lens. In the *Tg(ins:GCaMP6s);Tg(ins:cdt1-*  
155 *mCherry)* double-transgenic animals, we acquired the GCaMP6s and mCherry signals  
156 simultaneously using the 488nm and 561nm laser lines. The GCaMP6s signal was rendered  
157 in green and the nuclear signal in red. Videos were recorded at a 10 s/image (0.1 Hz) frame  
158 rate unless indicated otherwise, with a Z-step thickness of 1.2  $\mu\text{m}$ , covering on average 35  
159  $\mu\text{m}$ , and an XY resolution of 0.12  $\mu\text{m}$  per pixel (512x512 pixels). Laser power was  
160 maintained as low as possible (<1.5%) to minimise phototoxicity. For faster imaging, we  
161 focused on a single plane, recording a frame every 300 milliseconds with an XY resolution of  
162 0.08  $\mu\text{m}$  per pixel (512x512 pixels).

163

#### 164 *Zebrafish fast whole islet live imaging.*

165 Whole islet live-imaging at an acquisition rate of 0.8Hz, covering  $\sim 700\mu\text{m}^3$ , was achieved  
166 using resonant scanner technology with an inverted laser scanning confocal system (Leica  
167 SP5 MP) using an IRAPO L 25X/N.A. 0.95 water lens. Videos were recorded at  $\sim 0.8$  Hz per  
168 Z-stack ( $\sim 700\mu\text{m}^3$ ), with a Z-step thickness of 4.5  $\mu\text{m}$ , covering on average 70  $\mu\text{m}$  in depth,  
169 and an XY resolution of 0.24  $\mu\text{m}$  per pixel (256x256 pixels). The resonant scanner was set  
170 at 8,000 Hz with a bidirectional line scanning in order to achieve maximum speed.

171

#### 172 *Selective two-photon laser ablation of leader cells.*

173 Live imaging and intra-cardiac glucose injections were performed as described above using  
174 *Tg(ins:gCaMP6s;cryaa:mCherry)*, *Tg(ins:cdt1-mCherry;cryaa:GFP)* larvae. Images were  
175 captured across a single confocal plane at an imaging acquisition rate of six frames/second  
176 (6Hz). We performed three independent injections of glucose, separated by 5 min. intervals.  
177 The “leader cell” (that is the temporally-defined first responder) was identified by eye based  
178 on the changes in GCaMP6s-fluorescence after each glucose-injection. The larvae were  
179 then transferred to a Leica SP5 MP confocal microscope, equipped with a two-photon laser  
180 and 25X/0.95 N.A objective. A region of interest (ROI) was selected encompassing the  
181 center of the nucleus of the cell to be ablated, covering a circle with an approximate  
182 diameter of 0.5  $\mu\text{m}$ . The cell of interest was then exposed to two-photon laser irradiation at  
183 the output power of 2.0 W ( $\lambda = 800$  nm) for 5 s to minimize possible damage to other areas.  
184 We then performed live imaging and intra-cardiac injection again, using the protocol above,  
185 and within 20 min. of irradiation, to record the response following cell ablation. Control cells

186 that were not the temporally-defined first responders (“followers”) were ablated with the  
187 same methodology as leader cells. To ensure that the laser ablation technique was highly  
188 localised to a single cell, as expected with this approach, we fixed islets immediately after  
189 the laser cell-ablation (<10 min) then labelled them with insulin antibody and DAPI (see  
190 below).

#### 191 *Islet blood flow imaging in zebrafish.*

192 Imaging of islet blood flow was performed using triple transgenic larvae  
193 *Tg(ins:GCaMP6s);Tg(ins:cdt1-mCherry);Tg(gata1a:DsRed)*. *Tg(gata1a:DsRed)* reporter  
194 was used as a marker of red blood cells. Live imaging was performed on a ZEISS LSM 780  
195 confocal microscope equipped with a C-Apochromat 40X/1.2 NA water correction lens. The  
196 GCaMP6s and mCherry signals from  $\beta$  cells, and DsRed signals from blood cells, were  
197 simultaneously acquired using the 488nm and 561nm laser lines. The GCaMP6s signal was  
198 rendered in green. The blood cells and the nuclear signal of  $\beta$  cells were rendered in red.  
199 We focused on a single plane and the videos were recorded at a frame rate of 1 frame/155  
200 milliseconds (~6.4 Hz).

#### 201 *Mechanical heart stop in zebrafish.*

202 To stop the blood flow in zebrafish larvae, a glass-pulled pipette (3.5” Drummond #3-000-  
203 203-G/X, Sutter pipette puller P-1000), with a manually blunted end, was used to exert a  
204 direct pressure into the heart. The heart was blocked for around 400 s. The mechanical  
205 heart stopping was executed during live  $Ca^{2+}$  imaging in the *Tg(ins:GCaMP6s);Tg(ins:cdt1-*  
206 *mCherry)* double-transgenic larvae, as described above. Videos were recorded at a 10 s  
207 frame rate (0.1 Hz), and a Z-step thickness of 2.8  $\mu$ m, covering on average 50  $\mu$ m, with a  
208 frame size of 512 x 512 pixels.

#### 209 *Identification of dorsal- and ventral-bud derived $\beta$ cells.*

210 The primary zebrafish islet contains both dorsal bud-derived  $\beta$  cells (DBC) and ventral bud-  
211 derived  $\beta$  cells (VBC). To interrogate whether embryonic derivation affected the identity of  
212 leader cells, we performed injection of mRNA encoding H2B-RFP to distinguish between D-  
213 and VBCs based on label dilution<sup>34</sup>. In this assay, DBCs retain the H2B-RFP label whereas  
214 VBCs dilute it. We injected one-cell stage embryos with mRNA expressing H2B-mCherry.  
215 We maxi-prepped the pCS2+H2B-mCherry plasmid, digested it with KpnI and in vitro  
216 transcribed it using the SP6 Transcription Kit (Ambion, AM1340) to generate mRNA. We  
217 injected 100pg of H2B-mCherry mRNA in each embryo. Larvae were mounted as described  
218 above for whole islet live imaging and glucose-injections.

219 *Post mortem staining for cell ablation in zebrafish.*

220 After the live imaging was performed, and the leader cells were temporally identified, the  
221 larvae were immediately fixed in 4% PFA overnight. Then the samples were permeabilized  
222 with 1% PBT (Triton-X-100) for 1hr. To avoid non-specific primary antibody binding, we  
223 blocked for 2hrs in PBTB (PBT + 4% BSA). Nuclear staining was performed using DAPI at  
224 1:1000 dilution. After the immunostaining with anti-insulin (polyclonal guinea pig anti-Insulin,  
225 Dako A0564, 1:300 dilution), the samples were mounted in Vectashield. The anti-insulin  
226 antibody has been previously validated to mark  $\beta$ -cells in zebrafish by us using transgenic  
227 lines that express GFP under the insulin promoter and was also recently validated to show  
228 negative immunoreactivity in  $\beta$ -cells in homozygous mutant fish for the *insulina* gene (PMID:  
229 30520733), confirming its high specificity. Images were acquired using Z-Stacks on a LSM-  
230 780 Zeiss confocal microscope. For image analysis, the nuclei of the  $\beta$  cells were  
231 segmented using the DAPI channel.

232

233 *Ex vivo imaging of primary and secondary zebrafish islets.*

234 The islet culture and imaging were performed as previously described<sup>35</sup>. Primary and  
235 secondary islets were isolated from three month post fertilization (mpf) *Tg(ins:gCaMP6s;*  
236 *cryaa:mCherry)* animals. The islets were stimulated with a ramp of 10 and 20 mM D-glucose  
237 (Sigma, G8270). The imaging culminated with the addition of 30mM KCl (Sigma, P9451) in  
238 the same plate. Videos were recorded at a 2.5 s/image (0.25 Hz frame rate), in a single Z-  
239 plane and with an XY resolution of 0.59  $\mu$ m per pixel (1024x1024 pixels). After imaging,  
240 individual  $\beta$  cell ROIs were manually drawn using Image J. Fluorescence intensity (FI) was  
241 normalized using the minimum and maximum values of FI across frames for each cell. Cells  
242 which did not show an increase in GCaMP signal after KCl addition, were not included in the  
243 analysis.

244

245 *Image analysis from in vivo imaging of zebrafish.*

246

247 The cumulative population response of  $\beta$  cells was quantified from maximum intensity  
248 projections (MIP) of the z-stack. In the MIP, the islet area was delimited manually using the  
249 Region of Interest (ROI) Manager in ImageJ (<https://imagej.net/Fiji>)<sup>36</sup>. Using the ROI, the  
250 integrated fluorescence intensity of GCaMP6s was extracted. The integrated fluorescence  
251 intensity was normalized for the whole imaging time using the following formula:

252

253  $(F_T - F_{MIN}) / (F_{MAX} - F_{MIN}),$

254



255 where  $F_T$  is the integrated fluorescence intensity at a given time while  $F_{MAX}$  and the  $F_{MIN}$  are  
256 the maximum and minimum values recorded during the live imaging session, respectively.

257

258 Single-cell signal analysis of GCaMP signal was performed either from single-confocal slices  
259 covering a majority of imaged  $\beta$  cells (2D) or by segmenting the nuclei from the Z-stacks  
260 using the nuclear mCherry signal (3D). For nuclear segmentation, we utilized the 3D image  
261 suite in Image J, and the 3D iterative thresholding plugin<sup>37</sup>. The following parameters were  
262 set based on the estimated approximate nuclear size of  $\beta$  cells: minimum volume = 100  
263 pixels; maximum volume = 1200 pixels; criteria method = “volume”; threshold method =  
264 “volume”; value method = 10 units. This generated a voxel covering the nuclei of  $\beta$  cells.  
265 Using the 3D ROI manager plugin, we extracted the integrated fluorescence intensity from  
266 each voxel over time (FT). In order to create 3D plots, we first extracted the centroids from  
267 each voxel and then plotted them using the R software and the package “rgl”. Single-cell  
268 heat-maps based on 2D analysis were created using Excel and conditional formatting setting  
269 the colors in a gradient from 0 to 1. For visualization, the brightness and contrast was  
270 adjusted uniformly across the times series using ImageJ, and the tool Brightness/Contrast.

271

272 *Quantification of GCaMP6s fluorescence intensity in zebrafish images.*

273 For the quantification of changes in GCaMP6 fluorescence upon glucose or insulin injection  
274 in Figure 1 and Supplementary Figure 1, the cumulative response of all imaged  $\beta$ -cells to  
275 glucose injection was quantified. To this end, we compared the area under the curve based  
276 on the normalized integrated fluorescence intensity 10 frames before and after the injections  
277 of glucose or insulin (covering 200 seconds of imaging) using the formula:

278

$$279 (F_T - F_{MIN}) / (F_{MAX} - F_{MIN}),$$

280

281 For the quantification of changes in GCaMP6 fluorescence upon laser-cell ablation (Figure  
282 4), the cumulative response of all imaged  $\beta$  cells to glucose injection was quantified. In this  
283 case, the maximum value ( $F_{MAX}$ ) was not used for normalization since such normalization  
284 could mask the effect of loss of response following cell ablation due to normalization to  
285 background fluorescence. Instead, we only subtracted the background from the imaging  
286 session using the following formula:

287

$$288 (F_T - F_{MIN}) / F_{MIN}$$

289

290 The larvae were injected with three separate pulses of glucose before and after the ablation.  
291 For each injection the GCaMP area under the curve was calculated covering 200 frames

292 after the glucose injection. The average area under the curve was calculated before and  
293 after the ablation and plotted as  $\log_2$ .

294

#### 295 *Spatial drift correction OF ZEBRAFISH images.*

296 The red channel (cdt1-mCherry) signal from the  $\beta$  cell nuclei was used to correct for spatial  
297 drift in the green GCaMP6s channel. A maximum projection of each Z-stack in the time  
298 series was entered into the FIJI plugin “Descriptor-based series registration (2d/3d + t)”  
299 ([https://imagej.net/Descriptor-based\\_registration\\_\(2d/3d\)](https://imagej.net/Descriptor-based_registration_(2d/3d)))<sup>38</sup>, applying the model “Rigid (2d)”,  
300 with “3-dimensional quadratic fit”. A sigma of 13 and threshold of 0.03 was applied to the  
301 detection of nuclear signal, with a minimum number of three neighbors, redundancy of 1 and  
302 a random sample consensus (Ransac) error of 5. Matching across time series was achieved  
303 using global optimization, unless indicated otherwise. Stabilization in the Z dimension was  
304 achieved using the Fiji “Reslice” command. The “Descriptor-based series registration (2d/3d  
305 + t)” plugin was used with nuclei detection sigma set to 5 and with a threshold of 0.03.

306

307

#### 308 *Mouse husbandry.*

309 Male C57Bl/6 wild type (WT) (18-25g) mice were purchased from Charles River, UK, and  
310 used as donor islet recipients. For *in vivo* measurements of cytosolic  $\text{Ca}^{2+}$  in pancreatic  $\beta$   
311 cells, we generated mice that express GCaMP6f in  $\beta$  cells using the Cre-Lox system. Briefly,  
312 we crossed Ins1Cre mice (provided by J Ferrer, this Department)<sup>39, 40</sup> with mice that express  
313 GCaMP6f downstream of a LoxP-flanked STOP cassette (The Jackson Laboratory, stock  
314 no. 028865). Islets donated from either sex were used for transplantation. Mice were  
315 housed in groups of six in individually-ventilated cages under controlled conditions (21-23°C;  
316 12 h light: 12 h dark cycle). Male BALBc *nu/nu* (The Jackson Laboratory, stock no. 002019)  
317 recipients were used for human islet transplantation. Animals had *ad libitum* access to  
318 standard chow and water (irradiated for the immunocompetent mice). All animal procedures  
319 were approved and performed under the UK Home Office Animals (Scientific Procedures)  
320 Act 1986 (Project License to I.L., PA03F7F07 at Imperial College London. The project  
321 licence received internal institutional ethical approval as well as external Home Office  
322 approval).

#### 323 *Generation of adenovirus expressing GCaMP6m (AV-GCaMP6m).*

324 A plasmid driving the expression of *GCaMP6m* under the control of the cytomegalovirus  
325 (CMV) promoter (CMV-AVGCaMP6m) was generated using the pAdEasy system<sup>41</sup>. Briefly,  
326 pGP-CMV-GCaMP6m plasmid (Addgene plasmid # 40754) was digested using *Bgl*II and

327 *Notl.* The released GCaMP6m fragment was then purified and ligated into pShuttle-CMV  
328 vector (Addgene plasmid # 16403). CMV-GCaMP6m was inserted by recombination into the  
329 adenoviral pAdEasy-1 vector (Addgene plasmid # 16400), and transformed into  
330 electrocompetent BJ5183 cells. The isolated plasmid was subsequently amplified in reduced  
331 recombination rate (recA1) NEB-10 $\beta$  competent *E. coli* (New England BioLabs). Following  
332 the transfection of AD293 cells with the linearized pAdEasy-CMV-GCaMP6m construct, cells  
333 were harvested and lysed to release virions. The virus was further amplified and purified by  
334 centrifugation on a CsCl gradient. Titration was performed by infecting AD293 cells with  
335 serially diluted viral stocks, counting positive cells through GCaMP6m fluorescence.

336 *Islet transplantation into murine anterior chamber of the eye (ACE).*

337 Pancreatic islets were isolated and cultured as described previously <sup>42</sup>. For transplantation,  
338 10-20 islets were aspirated with a 27-gauge blunt eye cannula (BeaverVisitec, UK)  
339 connected to a 100ul Hamilton syringe (Hamilton) via 0.4-mm polyethylene tubing (Portex  
340 Limited). Prior to surgery, mice were anaesthetised with 2-4% isoflurane (Zoetis) and placed  
341 in a stereotactic frame to stabilise the head. The cornea was incised near the junction with  
342 the sclera, being careful not to damage the iris. Then, the blunt cannula, pre-loaded with  
343 islets, was inserted into the ACE and islets were expelled (average injection volume 20  $\mu$ l for  
344 10 islets). Carprofen (Bayer, UK) and eye ointment were administered post-surgery.

345 *In vivo Ca<sup>2+</sup> imaging of AV-GCaMP6m infected murine islets in the ACE.*

346 Prior to transplantation into the ACE of recipients, isolated islets (from WT C57/BL6 donors,  
347 <24 weeks old or human islet donations) were infected with AV-GCaMP6m *in vitro* at a  
348 multiplicity of infection (MOI) of 20 for 24 h. This approach, which was expected to allow the  
349 identification, if present, of functional islet sub-compartments (i.e. local groups of interacting  
350  $\beta$  cells) provided preferential infection of superficial  $\beta$  cells (1-2 cells deep). Of these, ~ 50 %  
351 were infected. A minimum of four weeks was allowed for full implantation of transplanted  
352 islets before imaging. Imaging sessions were performed with the mouse held in a  
353 stereotactic frame and the eye gently retracted, with the animal maintained under 2-4%  
354 isoflurane anaesthesia. All imaging experiments were conducted using a spinning disk  
355 confocal microscope (Nikon Eclipse Ti, Crest spinning disk, 20x water dipping 1.0 NA  
356 objective). The signal from AV-GCaMP6m fluorophore (ex. 488 nm, em. 525 $\pm$ 25 nm) was  
357 monitored in time-series experiments for up to 20 min. at a rate of 1 frame/sec. Ca<sup>2+</sup> traces  
358 were recorded for three min. prior to intraperitoneal (IP) glucose injection, with a mean blood  
359 glucose reading (across five islets in five separate animals) of 8 mmol/L. Three minutes into  
360 acquisitions mice received 150  $\mu$ l 30% (1.5g/kg) bolus of glucose intra-peritoneally (IP).  
361 Blood glucose was subsequently measured on a glucometer (Accu-Chek, UK) at two-minute

362 intervals from a tail vein nick until the end of experiments. Injection of glucose at 180 s  
363 raised blood glucose to an average of 28 mM for the remainder of the 10 min. imaging  
364 series. Since the mouse imaging experiments are the first of their kind, sample size ( $n=5$   
365 islets in  $n=5$  animals) was determined to be adequate based on the magnitude and  
366 consistency of measurable differences between groups. This was in line with other studies  
367 examining islets in the ACE <sup>22</sup>.

368

369 *In vivo Ca<sup>2+</sup> imaging of Ins1Cre-GCaMP6f islets in the ACE.*

370 Ins1Cre-GCaMP6f (ex.: 488nm, em. 525±25 nm) -expressing islets were isolated and  
371 transplanted into WT recipients ( $n=5$  islets in  $n=5$  different animals), and imaged as  
372 described above. Stream acquisitions of a single  $x/y$  plane of  $\beta$  cells recorded 2 min.  
373 datasets at 3Hz. Islets ( $n=5$  islets in  $n=5$  different animals) were continuously monitored and  
374 the focus was manually adjusted to counteract movement. Islets (in the same imaging  
375 session) were imaged under both “low glucose” (2–6 mM) and “high glucose” (17-25 mM)  
376 conditions (randomly ordered). Blood glucose (tail nick, Accu-chek glucometer) was  
377 assessed at 2 min. intervals throughout. Low glucose readings were obtained following the  
378 intravenous (IV) administration of insulin (Actrapid, 0.3ml of 1.0 iu/ml), and high glucose was  
379 achieved with a 200  $\mu$ l 30% (2g/kg) IP bolus of sugar. At the end of experiments animals  
380 were allowed to recover and were further monitored for an hour for potential post-operative  
381 latent hypoglycaemia.

382 To extend the image acquisitions to collect 3-dimensional data (ie. three separate planes of  
383  $\beta$  cells across an islet), a piezo device was attached to the inverted objective. This allowed  
384 for rapid, precise, 15  $\mu$ m z-movements such that a 3-slice z-stack could be obtained at a  
385 whole-islet imaging rate of 1 fps. At this imaging speed, we were able to obtain 3D  
386 connectivity readouts for low and high glucose conditions (as described above,  $n=3$  islets in  
387  $n=3$  different animals). As we became more expert with the ability of our platform, this  
388 number of experiments was sufficiently powered to demonstrate the rise in connectivity from  
389 low to high glucose in the 3D imaging experiments,

390

391 Finally, we examined islet Ca<sup>2+</sup> dynamics during a longer period of glucose stimulation, to  
392 exclude the possibility that pan-islet connectivity is related to spatially aggregated  $\beta$  cells  
393 simply responding acutely and synchronously to a rise in circulating glucose concentration.  
394 Five animals (five separate islets studied, in line with former acute experiments) were placed  
395 under isoflurane anaesthesia for 60 minutes. At the start of the imaging session an IP  
396 bolus of sugar was administered. This led to a slow and sustained rise in circulating blood

397 sugar (measured every 3-5 minutes via tail vein sampling, as before). 30-50 minutes into  
398 this imaging session, a 10-minute single plane islet recording was taken at 1fps, manually  
399 readjusted in real time for movement. This was performed at “high” glucose levels (i.e. when  
400 blood sugar levels had risen after IP glucose injection to a high, steady level >12 mmol/L).  
401 We also report connectivity at a previous stage in the imaging session (10-20 minutes in)  
402 when circulating glucose levels were at an intermediate (medium glucose, 7-10 mmol/L)  
403 range (but the islets were still exhibiting coordinated wave activity). In the same imaging  
404 session, the islets were recorded following IV administration of insulin when circulating levels  
405 of glucose were low (< 4 mmol/L). The same islet plane and  $\beta$  cell ROIs were investigated  
406 under each of the three (low, medium and high) circulating glucose conditions. To ensure  
407 that the findings from this experiment were unaltered with the use of another anaesthetic, we  
408 repeated these experiments using ketamine (Zoetis) and xylazine (Bayer) (90 mg/kg and 4.5  
409 mg/kg cocktail respectively), with similar findings.

#### 410 *In vivo Ca<sup>2+</sup> imaging of AV-GCaMP6m infected human islets*

411 We studied the behaviour of 11 individual human islets (four individual donors, age range  
412 14-74 years, non-diabetic, BMI range 21.5 to 29.2; see Supplementary Figure 5) that had  
413 been transduced with AV-GCaMP6m and transplanted into the ACE of  
414 (immunocompromised) BALB/c *nu/nu* mice. A human donor with diabetes (female, 54 years  
415 old, BMI 24.4, type 2 diabetic for 10 years, insulin dependent for the last 1.5 yrs) provided  
416 islets for two experiments (separate islets in separate BALB/c *nu/nu* recipients). Human  
417 islets were obtained from multiple institutions (co-authors AMJS at the University of Alberta,  
418 Edmonton, Canada and PM at the University of Pisa, Italy). Permission for the use of  
419 human tissue was provided at Imperial College by the Charing Cross Research Ethics  
420 Committee, REC reference number 07/H0711/114. Human islets were obtained post  
421 mortem with next of kin and local and ethical permission at the sites of procurement. There  
422 was no selection procedure for the implantation of human donor islets, and they were  
423 implanted into recipient mice as they became available. Donor data are fully anonymised  
424 and no clinical data beyond age, gender, and cause of death were available.

425 Following an imaging protocol described for the *Ins1Cre-GCaMP6f* mouse studies above, we  
426 measured human islet behaviour under imposed low (< 4 mM) and high (>7 mM) glucose  
427 conditions. Since BALB/c mice are resistant to glucose rises under anaesthesia, there are  
428 more successful imaging results in the low glucose state reported. *Image analysis.* Using  
429 FIJI (Image J) software (see above), images in the time series were individually time  
430 stamped, to maintain their absolute time information, before excluding frames where  
431 resolution was poor or blurred by movement. Image series were then cropped and manually

432 aligned across all frames using a pre-defined region of interest (ROI) as reference. Creating  
433 ROIs for analysis was guided by the emitted GCaMP fluorescence and the negative shadow  
434 of nuclei. For the virally infected islets each ROI extended over the entirety of a cell, whereas  
435 ROIs in experiments with transgenic islets covered sub-cellular regions in close proximity to  
436 nuclei. Mean fluorescence intensity and XY(Z) co-ordinates for each cell within an islet  
437 (ROIs) were compiled and processed for connectivity analysis.

#### 438 *Pearson (R)-based connectivity analyses.*

439 Correlation analyses between the  $\text{Ca}^{2+}$  signal time series for all cell pairs in an imaged islet  
440 were performed in MATLAB using a custom-made script (available upon request). Data  
441 were smoothed using a retrospective averaging method (previous 10 values) and all traces  
442 were normalised to F0. Two-sided averaging techniques were not applied as this would  
443 have invalidated subsequent causality analyses. The correlation function R between all  
444 possible (smoothed) cell pair combinations (excluding the autocorrelation) was assessed  
445 using Pearson's correlation. Data are displayed as heatmap matrices, indicating individual  
446 cell pair connections on each axes (min. = -1; max. = 1). Given that data were not normally  
447 distributed (and hence resorting to either asymptotic p-values or Monte Carlo based ones  
448 would not be useful), the data were subsequently subjected to a bootstrap resampling to  
449 increase the accuracy of the confidence interval of the R statistic, and  $p < 0.001$  was deemed  
450 a statistically significant cell-cell connection. The Cartesian co-ordinates of the imaged cells  
451 were then taken into account in the construction of connectivity line maps. Cell pairs ( $R > 0.25$   
452 AND  $p < 0.001$  post bootstrap) were connected with a straight line, the colour of which  
453 represented the correlation strength and was assigned to a colour-coded light-dark ramp  
454 ( $R = 0.25-0.5$  [green],  $R = 0.5-0.75$  [yellow],  $R = 0.75-1.0$  [red]). An average coefficient of  
455 positive connectivity was computed for each condition, by averaging the positive R values  
456 (excluding the auto-correlated cells) and the percentage of cells that were significantly  
457 connected to one another was elicited, for the purposes of group comparisons.

458 We have not examined the immediate upstroke of an acute IV bolus of glucose i.e. from a  
459 low to a high glucose setting. Consequently the "first responders" in the mouse datasets  
460 refer to the first  $\beta$  cells observed to fire in a train of calcium waves during a period of more  
461 prolonged elevated glucose.

#### 462 *Signal binarization and Monte Carlo analysis.*

463 To investigate what happens in the tail of the distribution, and go beyond the analysis of  
464 linear association provided by the Pearson correlation coefficient, we also looked at  
465 association between activity regimes. This analysis was performed as described previously

466 <sup>20, 21</sup>. In brief, cells were considered to be either “on” or “off” if the fluorescent signal  
467 exceeded a 20% noise threshold above baseline. Binarized data for each cell pair were  
468 assessed for co-synchronicity using the co-activity statistic  $C_{ij} = T_{ij}/(\sqrt{[T_i \cdot T_j]})$  where C is a co-  
469 activity coefficient (0 to +1),  $T_i$  and  $T_j$  represent the time spent in the active state for each  
470 given cell and  $T_{ij}$  represents the time during which both cells are active. Pairs were  
471 considered linked if their statistic displayed a higher than chance ( $p < 0.01$ ) probability of  
472 interaction *versus* a Monte Carlo permuted version of the binarized matrix dataset. A  
473 probability distribution function of these connections (pooled across five islets) was  
474 presented as a log-log plot to look for a power law relationship, the strength of which was  
475 quantified by the coefficient of determination ( $R^2$ )<sup>38</sup>.

#### 476 *Granger analysis.*

477 The mouse *Ins1Cre* GCaMP6f-expressing islet series were subjected to a Granger Causality  
478 analysis<sup>32, 33</sup>. Individual cell-cell pairs were separately analysed (time lag 1-3 secs,  $p < 0.001$ )  
479 with a Bonferroni multiple comparison test. Granger-defined leaders, i.e. those cells with the  
480 greatest number of causally-linked followers, were compared with the temporally-defined  
481 leaders whose firing (in the high glucose condition) preceded the remainder of the  $\beta$  cell  
482 population. Granger leaders that persisted when the low, medium and high glucose  
483 experiments were performed on the same network of  $\beta$  cells were spatially located on the  
484 islet map to understand their spatial distribution.

485

#### 486 *Zebrafish transcriptomic analysis (single cell RNAseq).*

487 For single-cell RNA-Seq of the zebrafish pancreatic cells using the 10x Genomics platform,  
488 cell suspension was prepared from primary islets of six 2 mpf *Tg(ins:BB1.0L)*<sup>26</sup> using the  
489 protocol described in<sup>43</sup> ( $n=6$  animals). The cell suspension was passed over a 30  $\mu$ m cell  
490 filter (Miltenyi Biotec, 130-041-407) to remove debris and cell-aggregates, adjusted with  
491 HBSS (without Ca, Mg) to a density of 800 cells/ $\mu$ l, and diluted with nuclease free water  
492 according to the manufacturer’s instructions to yield 5000 cells. Subsequently, the cells were  
493 carefully mixed with reverse transcription mix before loading the cells on the 10X Genomics  
494 Chromium system<sup>44</sup>. After the gel emulsion bead suspension underwent the reverse  
495 transcription reaction, emulsion was broken and DNA purified using Silane beads. The cDNA  
496 was amplified with 10 cycles, following the guidelines of the 10x Genomics user manual. The  
497 10X Genomics single cell RNA-seq library preparation – involving fragmentation, dA-Tailing,  
498 adapter ligation and indexing PCR – was performed based on the manufacturer’s protocol.  
499 After quantification, the libraries were sequenced on an Illumina NextSeq 550 machine using

500 a HighOutput flowcell in paired-end mode (R1: 26 cycles; I1: 8 cycles; R2: 57 cycles), thus  
501 generating ~45 mio fragments. The raw sequencing data was then processed with the  
502 'count' command of the Cell Ranger software (v2.1.0) provided by 10X Genomics with the  
503 option '--expect-cells' set to 5000 (all other options were used as per default). This yielded  
504 2625 cells. To build the reference for Cell Ranger, zebrafish genome (GRCz10) as well as  
505 gene annotation (Ensembl 87) were downloaded from Ensembl and the annotation was  
506 filtered with the 'mkgtf' command of Cell Ranger (options: '--  
507 attribute=gene\_biotype:protein\_coding --attribute=gene\_biotype:lincRNA --  
508 attribute=gene\_biotype:antisense'). Genome sequence and filtered annotation were then  
509 used as input to the 'mkref' command of Cell Ranger to build the appropriate Cellranger  
510 Reference.

511

### 512 *Cluster analysis.*

513 scRNA-Seq data from C57BL/6 mouse islets were downloaded from NCBI GEO  
514 (GSE84133)<sup>45</sup>. UMI-filtered counts were analysed using the Seurat package<sup>46</sup>. The data  
515 were filtered and normalised then highly variable genes identified for PCA analysis and  
516 graph-based clustering. In the mouse data, insulin, glucagon and somatostatin cells were  
517 largely separated into distinct clusters. The initial clustering of the fish data produced a  
518 single cluster containing cells expressing *ins*, *gcga* and *sst1.1* (listed by ENSEMBL as the  
519 zebrafish orthologue of the H. sapiens SST gene; similar data were obtained using the  
520 *sst1.2* gene). This 'endocrine' cluster was separated from the other cells and re-clustered,  
521 producing distinct clusters for these three genes. The *ins*+ clusters were combined and the  
522 few remaining cells positive for *gcga*, *sst1.1* or *gip*, or negative for *ins*, were excluded. Within  
523 this group of  $\beta$  cells, the intersection between the upper quartile of *gck* expression and lower  
524 quartile of *ins* expression was identified as putative hub cells, based on the properties of  
525 these cells described previously<sup>21</sup>. Genes differentially expressed between the putative hub  
526 cells and remaining  $\beta$  cells were identified using Wilcoxon rank sum test and the upregulated  
527 genes thus identified were tested for statistical overrepresentation of Gene Ontology (GO)  
528 BP terms using Pantherdb.org<sup>47</sup>. Insulin-positive mouse cells were analysed in a similar  
529 manner except that putative hub cells were classified as the intersection between the upper  
530 quartile of *Gck* expression and the lower two quartiles of *Ins1* expression.

531

### 532 *Statistical analysis.*



533 Statistical significance between two conditions was assessed using paired or unpaired  
534 Student's t-test. Interactions between multiple conditions were determined using one- or two-  
535 way ANOVA (with Tukey's or Bonferroni posthoc tests). Analyses were performed using  
536 Graph Pad Prism (GraphPad Software version 8.0) and MATLAB (Mathworks) and  
537 significant p-values are described in each relevant section. Values are plotted as mean  $\pm$   
538 SEM, unless otherwise stated.

539 *Data availability*

540 The data that support the findings of this study and the Matlab codes for the various  
541 connectivity analyses described above are available from the corresponding authors upon  
542 request. Zebrafish islet RNASeq data are deposited at the GEO repository with accession  
543 number GSE123662.

544

545

546

547

548

549 **RESULTS**

550 ***Glucose controls  $\beta$  cell connectivity in the living zebrafish.***

551 To explore  $\text{Ca}^{2+}$  dynamics *in vivo* with single-cell resolution we first imaged at low acquisition  
552 speeds (0.1 Hz; Supplementary Figure 1a) zebrafish larvae (4-5dpf) expressing GCaMP6s  
553 under the insulin promoter (Figure 1a) and the nuclear  $\beta$ -cell marker *Tg(ins:cdt1-mCherry)*,  
554 which marks  $86 \pm 6.6\%$  ( $n=5$  islets) of all  $\beta$ -cells at 5 dpf. We focused our study on the  
555 primary zebrafish islet, which is the only islet present at this stage. We first used *ex vivo*  
556 imaging to directly compare the glucose-responsiveness of the primary and secondary islets  
557 dissected from adult fish<sup>35</sup>. As expected,  $\beta$  cells from the primary and secondary islets  
558 showed apparent  $\text{Ca}^{2+}$  influx upon stimulation with 10 and 20 mM glucose or depolarization  
559 with potassium chloride (KCl;  $n=3$  primary and  $n=3$  secondary islets) (Supplementary Movie  
560 1). Thus, the primary islet is an adequate system for studying the glucose-stimulated  $\text{Ca}^{2+}$   
561 dynamics in zebrafish  $\beta$  cells, as well as representing the major site of insulin storage.

562

563 *In vivo* imaging of GCaMP6s-expressing  $\beta$  cells in larvae revealed the existence of  
564 endogenous oscillations in cytosolic free  $\text{Ca}^{2+}$  (12/12 animals studied; Supplementary Figure  
565 1 a-c, Supplementary Movie 2). This activity was inhibited by intracardiac injection of insulin,  
566 which lowered whole-animal glucose (Supplementary Figure 1, c-f, Supplementary Movie 3),  
567 indicating that the oscillatory  $\text{Ca}^{2+}$  signal was due to elevated circulating levels of glucose  
568 that are measurable by 4-5 dpf<sup>48</sup>.  $\text{Ca}^{2+}$  dynamics were also decreased after a transient  
569 suppression of blood flow by a temporally controlled heart block (Supplementary Movie 4).  
570 Time-lapse imaging of red-blood cells and  $\beta$  cells confirmed that the zebrafish islet is  
571 perfused in larvae (Supplementary Movie 5). Taken together, these results reveal  
572 endogenous  $\beta$  cell  $\text{Ca}^{2+}$  oscillations likely to be involved in the systemic sensing of glucose  
573 *in vivo* in the zebrafish.

574

575 We next explored the impact of increasing the levels of glucose in the zebrafish circulation.  
576 We performed intra-cardiac injection of glucose, allowing for rapid entry of the sugar into the  
577 circulation (Figure 1b-d). After a short lag (20-50 s) this manoeuvre led to a rapid increase in  
578 cytosolic  $\text{Ca}^{2+}$  concentrations (assessed as the time take to achieve a GCaMP6 signal >20%  
579 above baseline) in  $\beta$  cells across the islet (Figure 2 b-d; Supplementary Movie 6), and  
580 corresponded to the time-dependent increases in whole animal glucose concentrations  
581 assessed separately (Figure 1e).

582

583 We next sought to determine the degree to which the  $\beta$  cell population in these experiments  
584 was connected before and after stimulation with glucose, firstly at low imaging speeds of

585 0.1Hz (Figure 2 and Supplementary Figure 2) then at high imaging speeds of 3 Hz (Figure  
586 3a-d). We derived Pearson-based functional connectivity maps (see Methods) of pairwise  
587 comparisons between the  $\text{Ca}^{2+}$  traces of individual cells<sup>21, 49</sup>. At low imaging speeds, 10-  
588 15% of cells hosted a connection to another cell prior to glucose injection, and this rose  
589 significantly to ~50 % after glucose injection ( $p < 0.001$ , Figure 2 c-f). A similar, dramatic  
590 increase ( $p < 0.01$ ) was seen for connection strength (i.e. Pearson's correlation,  $R$ ; Figure  
591 2e). Of note, the temporally-defined "leader" cells (first responders to glucose stimulation)  
592 were amongst the most highly connected. For example, in the animal shown in Figure 2,  
593  $\text{Ca}^{2+}$  increases were first observed in two out of nine cells (cell 2 and cell 6; Figure 2b), and  
594 these cells were the most connected on Pearson analysis at high glucose (connected to  
595 seven or eight other cells out of a total of nine analysed; Supplementary Table 1).

596

597 Recorded at a higher acquisition rate (3 Hz) across a single plane,  $\beta$  cells again displayed  
598 modest connectivity at low glucose (pre-injection ~20%; Figure 3d). The increases in  
599 intracellular  $\text{Ca}^{2+}$  which followed glucose injection (Figure 3a and b) were associated with a  
600 significant rise in correlation coefficient (Figure 3c) as well as a marked increase in the  
601 number of functionally-connected cell pairs (post-injection ~88%,  $p < 0.0001$ , Figure 3d).  
602 Approached with a Pearson analysis at high glucose, essentially every cell became strongly  
603 connected to every other cell. Finally, whole islet live-imaging at an acquisition rate of  
604 0.8Hz, covering ~700 $\mu\text{m}^3$  was achieved. In this way, it was possible to resolve the majority  
605 (20) cells within the primary islet of the zebrafish (Figure 3e) and extract their signal spatially  
606 in three dimensions (Figure 3f; Supplementary Movie 7). We then undertook 3D connectivity  
607 analysis on three separate zebrafish islets before and after glucose stimulation (as before).  
608 Figure 3g shows the 3-dimensional connectivity analysis for one fish islet with mean  
609 coefficient of correlation rising from 40.1 to 89.1 and fraction of connected cells rising from  
610 11.2 to 92.3 % with a glucose bolus. Results for the other two islets showed the same rise in  
611 Pearson coefficient (83.2 to 91.7 and 44.9 to 85.1) and rise in connected cells (33.3 to  
612 55.5% and 16.7 to 38.1%). We therefore conclude that functional connectivity occurs across  
613 the entire fish islet and that 2-dimensional (single plane) connectivity analysis in the fish  
614 accurately reflects what occurs across the entire islet.

615

### 616 ***Ablation of leader cells prevents subsequent $\text{Ca}^{2+}$ waves in the zebrafish embryo.***

617

618 In order to determine whether "leader" (first responder) cells may serve a regulatory role, as  
619 demonstrated previously for mouse islets *in vitro*<sup>21</sup>, we used cell ablation through two  
620 photon laser irradiation (Figure 4, Supplementary Movies 8 and 9). Animals were challenged  
621 with three separate pulses of intracardiac glucose introduced before and after irradiation of

622 either leader or follower cells ( $n=20$  leader and  $n=20$  follower cell ablation experiments).  
623 Whereas ablation of follower cells had no discernible effect on the subsequent  $Ca^{2+}$  spikes,  
624 ablation of leader cells led to a significant reduction in the total islet GCaMP response  
625 (Figure 4). Only targeted cells revealed evidence of nuclear destruction, while the  
626 neighbouring cells showed no obvious damage (Supplementary Figure 4). Moreover, we  
627 show that islet blood flow remains unaltered following the ablation of the cells using bright-  
628 field imaging before and after the ablation (Supplementary Movies 8 and 9). Thus, the  
629 targeted ablation of a single  $\beta$  cell in vivo does not appear to perturb either local endothelial  
630 cells or the rest of the  $\beta$  cells in the islet.

631

632 ***Leader cells do not preferentially derive from the dorsal or ventral buds in the***  
633 ***zebrafish embryo.***

634

635 The primary zebrafish islet contains both dorsal bud-derived  $\beta$  cells (DBC) and ventral bud-  
636 derived  $\beta$  cells (VBC). To interrogate whether embryonic derivation affected the identity of  
637 leader cells, we performed injection of mRNA encoding H2B-RFP to distinguish between D-  
638 and VBCs based on label dilution<sup>34</sup>. In this assay, DBCs retain the H2B-RFP label whereas  
639 VBCs dilute it. We performed 4D live  $Ca^{2+}$  imaging and glucose injections in these embryos.  
640 In the three islets examined, two revealed label-retaining cells as leaders, meanwhile one  
641 islet revealed a leader cell that was H2B-negative. Supplementary Movie 10 shows a 3D  
642 reconstruction of one representative experiment in which the leader cell was H2B-RFP-  
643 positive. This implies that both the D- and VBCs can become leader cells. It is important to  
644 note that, in these experiments, we did not observe impaired responsiveness of DBCs to  
645 glucose stimulation *per se*, indicating that DBCs indeed exhibit characteristics of functional  $\beta$   
646 cells.

647

648 ***Glucose enhances  $Ca^{2+}$  dynamics and elicits increases in  $\beta$  cell- $\beta$  cell connectivity in***  
649 ***islets in the living mouse.***

650

651 We next extended our analysis to islets from the adult mouse, with superficial  $\beta$  cell layers  
652 infected with adenoviral GCaMP6m, before engraftment into the anterior chamber of a  
653 recipient mouse eye (ACE)<sup>22</sup>. Non- $\beta$  cells are not infected by this protocol due to the  
654 absence of the cognate receptor (Coxsackie virus receptor<sup>50</sup>). Using animals maintained  
655 under general anaesthetic, we collected data at acquisition speeds of 1 Hz, before and after  
656 IP glucose injection (see Methods).

657

658  $\text{Ca}^{2+}$  dynamics were increased in response to a rise in circulating glucose. The proportion of  
659 significantly Pearson-connected cells increased on average from  $38 \pm 11\%$  to  $65 \pm 9\%$  ( $n=5$   
660 islets in 5 animals,  $p=0.028$ ) with a non-significant ( $p=0.11$ ) rise in the mean coefficient of  
661 connectivity from  $0.54 \pm 0.03\%$  to  $0.63 \pm 0.04\%$ .

662

663 We subsequently generated islets from transgenic mice expressing GCaMP6f highly  
664 selectively in the  $\beta$  cell, under the control of *Cre* recombinase expressed from the *Ins1* locus  
665 <sup>39, 40</sup>, and transplanted into the mouse ACE as above. Almost every  $\beta$  cell ( $\sim 95\%$ ) <sup>21</sup> within  
666 the transgenic islet expressed the  $\text{Ca}^{2+}$  probe, allowing us to interrogate the activity of many  
667 more cells per islet, including those localised more deeply in the islet core (typically 50 to  
668 100). We captured data at higher rates (up to 3 Hz) under low and high circulating glucose  
669 conditions (see Methods).

670

671 Strikingly, and in contrast to islets infected with adenoviral GCaMP6f, we observed wave-like  
672 behaviour of the  $\beta$  cell  $\text{Ca}^{2+}$  increases in all islets (examined separately and in ten different  
673 animals) at high circulating glucose levels (Supplementary Movies 11, 12 and 13, Figure 5b  
674 and 6c).  $\text{Ca}^{2+}$  waves were initiated at discrete sites (Supplementary Movie 12), with  
675 propagation velocities of  $12.0 \pm 3.4 \mu\text{m/s}$  ( $n=5$  wave bursts). As shown in the example in  
676 Figure 5B and Supplementary Movie 13, whilst most cells were quiescent under low glucose  
677 conditions, high circulating glucose levels was associated with runs of highly-coordinated  
678 oscillations, even after prolonged glucose exposure (10 minutes, Figure 5b and Figure 6a).

679

680 We were able to quantify connectivity using both Pearson and binarized data approaches  
681 (Figures 5 and 6). As observed in the fish, high circulating glucose was associated with a  
682 significantly higher mean coefficient of connectivity, and proportion of connected cells,  
683 versus the low glucose condition, as revealed by Pearson analysis (Figures 5 c-e and  
684 Supplementary Figure 5a). We also used a piezo device to allow for fast acquisition of  $\beta$  cell  
685 readouts in three separate cell layers under low and high circulating glucose conditions, to  
686 investigate whether  $\beta$  cell connectivity existed in 3-dimensions (see Methods). Of note, this  
687 significant rise in pan-islet  $\beta$  cell connectivity at high circulating glucose levels also occurred  
688 between cells that were more than a layer apart on 3D imaging (Figure 5c-e and  
689 Supplementary Figure 5a). The Pearson analysis was, however, unable to detect significant  
690 differences in co-activities required for identification of super-connected cells/hubs. In  
691 contrast, application of a binarized approach (see Methods) <sup>21</sup> revealed scale free network  
692 topography in which  $8.7 \pm 3.7\%$  of cells hosted the majority (60-100%) of connections  
693 (Figures 6 a-b and Supplementary Figure 6). Pooled over all five islets examined, the  $R^2$   
694 value for this power law distribution was 0.62.

695

696 Finally, we examined islet  $\text{Ca}^{2+}$  dynamics over 10 minutes at steady state high glucose  
697 levels (and also acquired medium and low glucose acquisitions from the same cells in the  
698 same 1 h-long imaging study), to exclude the possibility that pan-islet connectivity is related  
699 to spatially aggregated  $\beta$  cells simply responding acutely and synchronously to a rise in  
700 circulating glucose concentration. Blood sugar readings recorded over these imaging  
701 sessions did not reveal oscillating glucose levels, excluding the trivial possibility that glucose  
702 oscillations themselves are driving  $\text{Ca}^{2+}$  oscillations (Figure 5b). A concerted, elevated  
703 Pearson correlation and percentage  $\beta$  cell connectivity was achieved over these longer  
704 acquisitions with higher (and sustained) circulating glucose levels (Figure 6a).

705

### 706 ***Prospective analysis (Granger causality)***

707

708 Given the challenges of a direct interventional strategy such as photo-ablation in the mouse  
709 eye, we deployed an alternative, mathematical approach to examine the potential role of  
710 leader cells as pacemakers. Granger analysis<sup>32</sup> provides a means of assessing whether a  
711 given time series may be useful in forecasting another, i.e. is predictive of a causal  
712 relationship. This supported our visual identification of first responding (leader) cells. As  
713 shown in Figure 6 c-e, we observed that those four cells (“leaders”, Figure 6C; this islet is  
714 shown in Supplementary Movie 11), which fired first during a prolonged run of  $\text{Ca}^{2+}$  pulses,  
715 were always represented as leaders in the second and third bursts but not always in fourth  
716 and fifth bursts (if present). However, leader cells identified temporally as among the first five  
717 responding cells under high glucose conditions were invariably the most highly connected on  
718 independent Granger analysis ( Supplementary Table 2). Granger analysis of the top 10  
719 most highly connected cells during the prolonged imaging sessions (10 minute acquisitions  
720 at high, medium and low glucose, of the same cross section of islet/same  $\beta$  cell ROIs)  
721 revealed one cell to be a Granger leader in all three states and, interestingly, to be in the  
722 same region (neighbouring) 2-5 other Granger leaders in the medium and high state – which  
723 was also the segment of islet from which waves emanated (data not shown).

724

725 Interestingly, this analysis provided no evidence that peri-capillary cells were more likely to  
726 be “Granger leaders” (average distance from leader cells to the nearest capillary:  $2.2 \pm 1.9$   
727  $\mu\text{m}$  versus  $2.3 \pm 1.8 \mu\text{m}$  for follower cells,  $n=25$ ,  $p>0.05$ ). Hence, differences between cells in  
728 the arrival time for glucose from the blood stream are unlikely to be the determining factor for  
729 initiating  $\text{Ca}^{2+}$  waves.

730

731 ***Engrafted human islets are highly connected.***

732

733 To corroborate our findings in a further species we studied the behaviour of 11 human islets  
734 transduced with AV-GCaMP6m and transplanted into the ACE of (immunocompromised)  
735 BALB/c *nu/nu* mice (see Methods) We observed a non-significant rise in human islet  
736 coefficient of correlation from 0.39 to 0.59, and a corresponding rise in  $\beta$  cell connectivity  
737 from 56% to 76% between low and high circulating glucose conditions (Supplementary  
738 Figure 5b). Intriguingly, in the two islets that came from a donor with longstanding Type 2  
739 Diabetes (see Methods), the switch from low to high circulating blood sugar was associated  
740 with an unexpected drop in Pearson R (53 to 24 and 44 to 32), and an equivalent fall in the  
741 proportion of connected  $\beta$  cells (from 30% to 20% and 29% to 27%; Supplementary Figure  
742 5c). This observation opens up the possibility that the loss of insulin secretory function that  
743 occurs in Type 2 diabetes is linked to abnormal connectivity patterns.

744

745 ***Transcriptomic analysis.***

746

747 To determine whether hub/leader cells may possess a discrete molecular signature *versus*  
748 followers we analysed RNASeq data from fish and mouse  $\beta$  cells. We have previously  
749 reported <sup>21</sup> that hub cells in the mouse islet are characterised by relatively high levels of  
750 glucokinase (Gck) immunoreactivity, and lower levels of Insulin, Pdx1, Nkx6,1 staining.

751

752 We first generated and analysed a zebrafish transcriptomic data set (10x Genomics) and  
753 were able to identify a cluster of mainly endocrine cells expressing *sst1.1*, *gcga* or *ins*.  
754 Further clustering of these 'endocrine' cells produced clusters of likely delta (*sst1.1*), alpha  
755 (*gcga*) and  $\beta$  (*ins*) cells (Supplementary Figure 6a-b). Putative hub cells were identified  
756 based on the higher glucokinase and lower insulin expression previously observed in mouse  
757 islets. The intersection of the upper quartile of *gck* expression and the lower quartile of *ins*  
758 expression identified 9 % of  $\beta$  cells as putative hub cells (Supplementary Figure 6c).  
759 Enrichment and gene ontology (GO) analysis revealed elevated expression of genes in  
760 hub/leaders associated with mitochondrial metabolism (oxidative phosphorylation and  
761 respiratory electron transport chain) and generation of precursor metabolites and energy,  
762 among other terms (Supplementary Figure 6 d-e). Interestingly, the re-clustering of the  
763 'endocrine' cluster resulted in two distinct and approximately equally-sized  $\beta$  cell  
764 populations. The putative hub cells identified here came almost entirely from a single cluster,  
765 suggesting these may represent one end of a continuous distribution within this cluster  
766 rather than a distinct subset.

767

768 Similar analysis of mouse islet data revealed that the intersection of the upper quartile of  
769 *Gck* and lower two quartiles of *Ins1* expression contained 11 % of  $\beta$  cells (Supplementary  
770 Figure 6 f-h). Genes upregulated in this cluster were overrepresented in the GO terms  
771 “Glycolysis” and “Generation of precursor metabolites and energy” (Supplementary Figure 6  
772 i-j), potentially indicating that these are more metabolically active cells, as observed above in  
773 the zebrafish case.

774

775

776

777



778 **DISCUSSION**

779

780 The principal aim of the present study was to explore  $\beta$  cell coordination in the islet *in vivo* in  
781 the living animal. Here, we have studied the zebrafish islet in its natural state and the mouse  
782 islet under conditions of vascularisation and innervation which closely recapitulate those of  
783 the islet within the pancreas<sup>51-53</sup>. We show that, despite the quite profound differences  
784 between the isolated and *in vivo* islet, coordinated  $\beta$  cell responses to glucose stimulation  
785 display many of the features previously described *in vitro*, including the emergence of cells  
786 which may govern islet-wide  $\text{Ca}^{2+}$  dynamics and hence pulsatile insulin secretion.

787

788 We demonstrate firstly that, in the zebrafish, increases in blood glucose lead to a  
789 coordinated increase in  $\beta$  cell cytosolic  $\text{Ca}^{2+}$  across the islet. Using Pearson R analysis, we  
790 describe a well-connected network of  $\beta$  cells in the zebrafish islet that responded in a  
791 coordinated fashion to glucose stimulation. These findings align well with those of Markovic  
792 *et al*<sup>49</sup> in murine pancreatic slices, and our own findings in isolated mouse islets<sup>18</sup>. Given  
793 the small size of the zebrafish islet at this developmental stage, it was not possible to apply  
794 scale-free network theory to these datasets. However, we were able, using a direct  
795 interventional approach akin to the use of optogenetics in isolated murine islets<sup>21, 54</sup>, to  
796 demonstrate that those cells which were the first to exhibit a  $\text{Ca}^{2+}$  increase (“leaders”) may  
797 perform a role as regulators of the activity of other  $\beta$  cells. Photo-ablation of leader, but not  
798 follower cells, resulted in a significant abrogation of  $\text{Ca}^{2+}$  dynamics in remaining  $\beta$  cells in  
799 terms of their time to response as well as their overall calcium response to a glucose  
800 challenge. We also provided evidence to establish that this methodology produced no  
801 collateral damage, i.e. did not affect cells other than the single  $\beta$  cell that was targeted. We  
802 would emphasize that this approach offers significant advantages over the use of  
803 optogenetics for  $\beta$  cell targeting, notably the fact that further genetic modification required to  
804 express an optogene (e.g. a photoswitchable channel or pump- shown to influence  $\beta$  cell  
805 activity)<sup>21, 54, 55</sup> is avoided, and axial resolution is high. Photo-ablation of leader, but not  
806 follower cells, resulted in the abrogation of  $\text{Ca}^{2+}$  dynamics (Fig. 4c), pointing to a role for the  
807 former as regulators of  $\beta$  cell activity across the islet.

808

809 It was particularly interesting to note the findings of the *ex vivo* imaging studies that directly  
810 compared *in vitro* glucose-responsiveness of the primary and secondary zebrafish islets.  
811 The only discernible difference we observed between the primary and the much later-  
812 forming secondary islets *ex vivo* pertained to a faster  $\text{Ca}^{2+}$  response of the latter, which was  
813 evident at 10 mM glucose. This faster response is likely to reflect the much smaller size of  
814 the secondary islets and, hence, the easier penetration to the islet core of glucose when

815 added *ex vivo*. It is important to note also that we have not observed impaired  
816 responsiveness to glucose stimulation of  $\beta$  cells originating from the dorsal pancreatic buds  
817 *in vivo*, consistent with our recent findings that DBCs are functional<sup>26</sup>. Finally, when imaged  
818 in culture, the zebrafish islets exhibit seemingly uncoupled behaviours, revealing the  
819 glucose-sensitivity of individual  $\beta$ -cells<sup>26,56</sup>. In contrast,  $\beta$ -cells show synchronized  
820 responses to glucose *in vivo* (this study and<sup>56</sup>). Thus, the unperturbed conditions of the *in*  
821 *vivo* environment might be critical for the coupling of  $\beta$ -cells.

822

823 In mammalian islets, we routinely observed clear trans-islet, glucose-induced  $\text{Ca}^{2+}$  waves  
824 (10/10 Ins1Cre-GCaMP6-expressing islets examined in independent experiments), whereas  
825 these are not always observed in Fluo8-loaded isolated islets *in vitro*<sup>21</sup>. This may reflect the  
826 presence of nerves and blood vessels in our *in vivo* model as well as, conceivably, the better  
827 preservation of  $\beta$  cell identity, gap junctions, etc.<sup>2</sup>. Moreover, the use of transgenic islets, in  
828 which the genetically-encoded  $\text{Ca}^{2+}$  sensor is present in almost the entire (~95%)  $\beta$  cell  
829 population after recombination using the Ins1Cre transgene<sup>21, 39, 40</sup>, is likely to facilitate the  
830 detection of waves. Thus, we were able to image cells located some distance away from the  
831 islet periphery, with adequate resolution to 4-5 cell depths in the z-plane (Supplementary  
832 Movie 14). Furthermore, with a rapid piezo device we were able to demonstrate that  $\text{Ca}^{2+}$   
833 dynamics were strongly coordinated across  $\beta$  cells that were separated by another layer of  
834 cells. However, the present studies do not address the question of how connections  
835 across the islet are established (e.g. roles for islet inter-neurons, paracrine factors, etc.).  
836 Other interventional approaches (e.g. using multiphoton, light sheet or other imaging  
837 techniques) will be necessary to explore these phenomena in the future.

838

839

840 By imaging large numbers of cells simultaneously, and subjecting the resulting datasets to  
841 binarization analysis, we revealed the existence of scale free networks, as previously  
842 described *in vitro*<sup>21</sup>. This set of experiments examined the nature of islet behaviour *in vivo*  
843 through two different but complementary lenses. Pearson R analysis highlights the pan-islet  
844  $\beta$  cell connectivity (both in terms of the number of connected cells and their strength of  
845 correlation) in response to elevated circulating glucose levels. Separately, we have  
846 demonstrated using data binarization and shuffling<sup>21</sup> that these cells are connected in a way  
847 that fits with the presence of super-connected hubs. Recently, Rupnik and colleagues<sup>57</sup>  
848 have reported, using mouse islets located within pancreatic slices, that at adequate  
849 acquisition speeds (10Hz), Pearson analysis can reveal a connectivity probability distribution  
850 function that obeys a power law, at least initially following glucose stimulation.

851

852 To corroborate our zebrafish findings, where disruption of the temporally-defined “leader”  
853 cells abrogated subsequent islet-wide  $\text{Ca}^{2+}$  responses to glucose, we performed  
854 independent mathematical causality analysis of all the  $\beta$  cells that were recorded in the  
855 mouse islet. Selecting a causality time lag consistent with that observed between the first  
856 responders and the rest of the  $\beta$  cells (i.e. 1 s)<sup>32</sup>, we revealed that these were indeed the  
857 most highly causally linked to the activity of all other cells in the islet. Both the experimentally  
858 established zebrafish “leaders” and the mathematically causally-identified mouse “leaders”  
859 are reminiscent of previously identified *in vitro* hub cells<sup>21</sup>, insofar as both regulate  $\text{Ca}^{2+}$   
860 dynamics observed in the rest of the islet being imaged. Our present findings also indicate  
861 that temporal and spatial dynamics need to be considered in identifying likely regulatory  
862 populations. For example, essentially normal blood flow is maintained in the engrafted islet.  
863 One may have predicted, therefore, that “leader”  $\beta$  cells would be those located immediately  
864 adjacent to blood vessels. In contrast, we observed no greater likelihood of cells in this  
865 domain of the islet initiating waves than for cells more remotely located. We also observed  
866 that islets retained a baseline  $\text{Ca}^{2+}$  activity (and indeed a degree of connectedness between  
867  $\beta$  cells) even in the low glucose state. Thus, at low circulating glucose levels  $\text{Ca}^{2+}$  waves  
868 were occasionally observed above noise levels with the same amplitude and frequency of  
869 bursts as at high glucose, but less commonly. Within a single train of waves, the starting  
870 point was often, but not always conserved, and was frequently seen at the islet rim. Such  
871 waves often propagated circumferentially, although there were some that appeared to move  
872 towards the islet core. Taken together, this hints that functional networks already exist at low  
873 glucose concentrations, under conditions in which the majority of cells are not yet firing.  
874 These pre-activated networks may then expand and work as a coordinating unit to drive the  
875 recruitment of followers.

876

877 It was also important to demonstrate a retention of the high connectivity readouts in islets  
878 that had been exposed to prolonged elevated glucose levels. Many previous studies on  
879 isolated islets and  $\beta$  cells reveal heterogeneous  $\text{Ca}^{2+}$  responses to glucose stimulation<sup>58</sup>.  
880 Indeed, we are not aware of existing literature supporting the notion that  $\beta$  cells have an  
881 identifiable (and identical) resting  $\text{Ca}^{2+}$  oscillation signature. Nevertheless, it was important  
882 here to exclude the possibility that the high connectivity observed at high glucose levels is a  
883 phenomenon related to spatially aggregated (i.e. intra-islet)  $\beta$  cells simply responding  
884 acutely and synchronously to a rise in circulating glucose concentration. The high  
885 connectivity findings in islets that had been imaged for an hour at elevated circulating  
886 glucose levels serve to argue against the possibility that connectivity is an acute

887 phenomenon of this type since, in an uncoordinated system, over a 60 min. imaging  
888 protocol, with glucose levels that are not rapidly varying, one would expect de-synchrony to  
889 emerge. Finally, the first responders (and Granger leaders) are defined during  $\text{Ca}^{2+}$  pulses  
890 at essentially constant glucose (although glucose may drift gradually over multiple  $\text{Ca}^{2+}$   
891 waves during these recordings).

892 Several questions remain with respect to the  $\text{Ca}^{2+}$  waves identified here: to what extent are  
893 their starting points spatially defined relative to nerves and other islet cell types? How do  
894 they propagate? Are they always associated with pulses of insulin secretion? Further studies  
895 are also required to determine whether “leader” cells are functionally essential to islet health,  
896 are pre-fated or can assume leader characteristics over time that relate to altered islet  
897 function under metabolic stress or in diabetes.

898

899 Prior to the current study, our understanding of the differences in molecular identity between  
900 hub and follower cells was fragmentary<sup>21</sup>. To explore this question here in an unbiased,  
901 transcriptome-wide manner, we have leveraged the known properties of mouse hub cells,  
902 i.e. elevated expression (at the protein level) of *Gck* and relatively weak expression of  
903 *Insulin*. We note that confirmation of similar properties for the fish hub/follower populations  
904 (i.e. high *Gck*low *insulin*low *Pdx1*-immunoreactivity) was not possible here due to the  
905 absence of suitable antibodies for the *D. rerio* *Gck* protein. Nonetheless, if we assume  
906 similar properties for the fish and mouse hub cells our analyses reveal that, in both species,  
907 a population exists with characteristics which may be expected of these cells, notably  
908 elevated expression of genes involved in glucose metabolism and, in zebrafish, of genes  
909 involved in mitochondrial metabolism. Of note, a similar  $\beta$  cell population was identified  
910 recently in the mouse by Pospisilik and colleagues<sup>59</sup>. Future studies, involving the direct  
911 isolation of hubs and followers based on function (e.g.  $\text{Ca}^{2+}$  dynamics), are needed to  
912 confirm or refute these findings.

913

914 In conclusion, we show here that examined in the living animal  $\beta$  cells within the islet are  
915 highly connected in three dimensions and that this connectivity is tightened in response to a  
916 glucose challenge. As predicted from previous studies of isolated islets *in vitro*<sup>18, 21</sup>, we  
917 show that critical subpopulations of  $\beta$  cells, which appear to generate  $\text{Ca}^{2+}$  waves, serve a  
918 regulatory role in the zebrafish and appear likely to do so in the mammalian islet as well. At  
919 this stage, it is not possible to investigate whether the leader cells are a distinct population  
920 with a distinct origin and development. However, we provide a preliminary analysis, using an  
921 imputation approach based on previously-described proteomic properties of these  
922 populations<sup>21</sup>, to suggest they possess a distinct transcriptomic signature. Future

923 challenges will involve isolating and characterising these cells, as well as assessing the  
924 stability of each sub group (i.e. leader/hubs and followers). Taken together, our data provide  
925 further evidence for a division of labour within the islet *in vivo* in three different species,  
926 reinforcing the importance of  $\beta$  cell heterogeneity for normal glucose-responsiveness.

927

## 928 **Acknowledgements.**

929

930 VS was supported by a Diabetes UK Harry Keen Clinician Scientist 15/0005317. G.A.R. was  
931 supported by a Wellcome Trust Senior Investigator Award (WT098424AIA), MRC  
932 Programme grants (MR/R022259/1, MR/J0003042/1, MR/L020149/1) and Experimental  
933 Challenge Grant (DIVA, MR/L02036X/1), MRC (MR/N00275X/1), Diabetes UK  
934 (BDA/11/0004210, BDA/15/0005275, BDA 16/0005485) and Imperial Confidence in Concept  
935 (ICiC) grants, and a Royal Society Wolfson Research Merit Award. I.L. was supported by  
936 Diabetes UK Project Grant 16/0005485 and D.J.H. by a Diabetes UK R.D. Lawrence  
937 (12/0004431) Fellowship, a Wellcome Trust Institutional Support Award, and MRC  
938 (MR/N00275X/1) and Diabetes UK (17/0005681) Project Grants. N.N. received funding from  
939 the DFG–Center for Regenerative Therapies Dresden, Cluster of Excellence at TU Dresden  
940 and the German Center for Diabetes Research (DZD), as well as research grants from the  
941 German Research Foundation (DFG), the European Foundation for the Study of Diabetes  
942 (EFSD) and the DZD. L.J.B.B. was supported by a Sir Henry Wellcome Postdoctoral  
943 Fellowship (Wellcome Trust, 201325/Z/16/Z) and a Junior Research Fellowship from Trinity  
944 College, Oxford. This project has received funding from the European Research Council  
945 (ERC) under the European Union’s Horizon 2020 research and innovation programme  
946 (Starting Grant 715884 to D.J.H.) and from the Innovative Medicines Initiative 2 Joint  
947 Undertaking under grant agreement No 115881 (RHAPSODY) to G.A.R. and P.M. This Joint  
948 Undertaking receives support from the European Union’s Horizon 2020 research and  
949 innovation programme and EFPIA. We would like to thank Professor Per-Olof Berggren  
950 (Karolinska Institute, Sweden and Imperial College London), Alejandro Caicedo and Raynor  
951 Rodriguez (University of Miami), and Drs Pauline Chabosseau, Marie-Sophie Nguyen-Tu  
952 and Bryn Owen (Imperial College London), for valuable advice and support with surgery and  
953 imaging. With thank Rebecca Callingham (Imperial College) for assistance with human islet  
954 culture.

955

956

957 **Author Contributions**

958 VS, NN and GAR designed the study, LDS and NA performed the zebrafish experiments,  
959 VS, KS, AMA, and IL undertook the mouse studies, GC and KS performed virus  
960 preparations, DCAG, SMR, KS and VS developed movement correction macros, EG,  
961 SNMG, NA, TS, DJH and LB contributed to connectivity analysis, DJH and LB provided code  
962 for connectivity analysis, VS and WD developed connectivity and Granger scripts and  
963 undertook all connectivity analyses, PM and AMJS provided human islets and KS and VS  
964 undertook studies on these preparations. TJP, NA and SPS performed transcriptomic and  
965 bioinformatics analyses. GAR, VS, LDS and NN wrote the manuscript with contributions from  
966 all authors.

967

968 G.A.R. has received grant funding from Servier and is a consultant for Sun Pharma. All  
969 others authors declare no competing financial interests

970

971

972

1. DeFronzo,R.A., Ferrannini,E., Zimmet,P., & Alberti,G. International Textbook of Diabetes Mellitus 4 th Edition. 2015. Hoboken, New Jersey, Wiley-Blackwell.

2. Rutter,G.A., Pullen,T.J., Hodson,D.J., & Martinez-Sanchez,A. Pancreatic beta cell identity, glucose sensing and the control of insulin secretion. *Biochem. J.* **466**, 202-218 (2015).

3. Tarasov,A.I. *et al.* The mitochondrial  $Ca^{2+}$  uniporter MCU is essential for glucose-induced ATP increases in pancreatic  $\beta$ -cells. *PLoS One* **7**, e39722 (2012).

4. Xin,Y. *et al.* RNA Sequencing of Single Human Islet Cells Reveals Type 2 Diabetes Genes. *Cell Metab.* **24**, 608-615 (2016).

5. Segerstolpe,A. *et al.* Single-Cell Transcriptome Profiling of Human Pancreatic Islets in Health and Type 2 Diabetes. *Cell Metab.* **24**, 593-607 (2016).

6. Li,J. *et al.* Single-cell transcriptomes reveal characteristic features of human pancreatic islet cell types. *EMBO Rep.* **17**, 178-187 (2016).

7. Wang,Y.J. *et al.* Single-Cell Transcriptomics of the Human Endocrine Pancreas. *Diabetes.* **65**, 3028-3038 (2016).

8. Kiekens,R. *et al.* Differences in glucose recognition by individual rat pancreatic B cells are associated with intercellular differences in glucose-induced biosynthetic activity. *J. Clin. Invest.* **89**, 117-125 (1992).

9. Ammala,C. *et al.* Inositol trisphosphate-dependent periodic activation of a  $Ca^{2+}$ -activated  $K^{+}$  conductance in glucose-stimulated pancreatic  $\beta$ -cells. *Nature* **353**, 849-852 (1991).

10. Benninger,R.K. & Piston,D.W. Cellular communication and heterogeneity in pancreatic islet insulin secretion dynamics. *Trends Endocrinol. Metab.* **25**, 399-406 (2014).

11. Meda,P. *et al.* The topography of electrical synchrony among beta-cells in the mouse islet of Langerhans. *Q. J. Exp. Physiol.* **69**, 719-735 (1984).

12. Palti,Y., David,G.B., Lachov,E., Mida,Y.H., & Schatzberger,R. Islets of Langerhans generate wavelike electric activity modulated by glucose concentration. *Diabetes.* **45**, 595-601 (1996).

13. Benninger,R.K., Zhang,M., Head,W.S., Satin,L.S., & Piston,D.W. Gap junction coupling and calcium waves in the pancreatic islet. *Biophys. J.* **95**, 5048-5061 (2008).

14. Head,W.S. *et al.* Connexin-36 gap junctions regulate in vivo first- and second-phase insulin secretion dynamics and glucose tolerance in the conscious mouse. *Diabetes.* **61**, 1700-1707 (2012).



- 1011 15. Meda,P., Kohen,E., Kohen,C., Rabinovitch,A., & Orci,L. Direct  
1012 communication of homologous and heterologous endocrine islet cells in culture.  
1013 *J. Cell Biol.* **92**, 221-226 (1982).
- 1014 16. Meda,P., Santos,R.M., & Atwater,I. Direct identification of  
1015 electrophysiologically monitored cells within intact mouse islets of Langerhans.  
1016 *Diabetes* **35**, 232-236 (1986).
- 1017 17. Rutter,G.A. & Hodson,D.J. Beta cell connectivity in pancreatic islets: a type 2  
1018 diabetes target? *Cell Mol. Life Sci.* **72**, 453-467 (2015).
- 1019 18. Hodson,D.J. *et al.* Lipotoxicity disrupts incretin-regulated human beta cell  
1020 connectivity. *J. Clin. Invest.* **123**, 4182-4194 (2013).
- 1021 19. Stozer,A. *et al.* Functional connectivity in islets of Langerhans from mouse  
1022 pancreas tissue slices. *PLoS Comput. Biol.* **9**, e1002923 (2013).
- 1023 20. Hodson,D.J. *et al.* Existence of long-lasting experience-dependent plasticity in  
1024 endocrine cell networks. *Nat. Commun.* **3**, 605 (2012).
- 1025 21. Johnston,N.R. *et al.* Beta cell hubs dictate pancreatic islet responses to  
1026 glucose. *Cell Metabolism* **24**, 389-401 (2016).
- 1027 22. Speier,S. *et al.* Noninvasive in vivo imaging of pancreatic islet cell biology.  
1028 *Nat. Med.* **14**, 574-578 (2008).
- 1029 23. Tian,L. *et al.* Imaging neural activity in worms, flies and mice with improved  
1030 GCaMP calcium indicators. *Nat. Methods.* **6**, 875-881 (2009).
- 1031 24. van der Meulen,T. *et al.* Virgin Beta Cells Persist throughout Life at a  
1032 Neogenic Niche within Pancreatic Islets. *Cell Metab.* **25**, 911-926 (2017).
- 1033 25. Chen,C. *et al.* Alterations in beta-Cell Calcium Dynamics and Efficacy  
1034 Outweigh Islet Mass Adaptation in Compensation of Insulin Resistance and  
1035 Prediabetes Onset. *Diabetes.* **65**, 2676-2685 (2016).
- 1036 26. Singh,S.P. *et al.* Different developmental histories of beta-cells generate  
1037 functional and proliferative heterogeneity during islet growth. *Nat. Commun.* **8**,  
1038 664-00461 (2017).
- 1039 27. Kimmel,R.A. & Meyer,D. Zebrafish pancreas as a model for development and  
1040 disease. *Methods Cell Biol.* **134**, 431-461 (2016).
- 1041 28. Steiner,D.J., Kim,A., Miller,K., & Hara,M. Pancreatic islet plasticity:  
1042 interspecies comparison of islet architecture and composition. *Islets.* **2**, 135-145  
1043 (2010).
- 1044 29. Bosco,D. *et al.* Unique arrangement of alpha- and beta-cells in human islets  
1045 of Langerhans. *Diabetes.* **59**, 1202-1210 (2010).
- 1046 30. Prince,V.E., Anderson,R.M., & Dalgin,G. Zebrafish Pancreas Development  
1047 and Regeneration: Fishing for Diabetes Therapies. *Curr. Top. Dev. Biol.* **124**:  
1048 235-276 (2017).

- 1049 31. Ninov,N. *et al.* Metabolic regulation of cellular plasticity in the pancreas. *Curr.*  
1050 *Biol.* **23**, 1242-1250 (2013).
- 1051 32. Granger,C.W.J. Investigating Causal Relations by Econometric Models and  
1052 Cross-spectral Methods. *Econometrica* **37**, 424-438 (1969).
- 1053 33. Barnett,L. & Seth,A.K. The MVGC multivariate Granger causality toolbox: a  
1054 new approach to Granger-causal inference. *J. Neurosci. Methods.* **223**, 50-68  
1055 (2014).
- 1056 34. Hesselson,D., Anderson,R.M., Beinat,M., & Stainier,D.Y. Distinct populations  
1057 of quiescent and proliferative pancreatic beta-cells identified by H0Tcre mediated  
1058 labeling. *Proc. Natl. Acad. Sci. U. S. A.* **106**, 14896-14901 (2009).
- 1059 35. Janjuha,S., Pal,S.S., & Ninov,N. Analysis of Beta-cell Function Using Single-  
1060 cell Resolution Calcium Imaging in Zebrafish Islets. *J. Vis. Exp.*10 (2018).
- 1061 36. Schindelin,J. *et al.* Fiji: an open-source platform for biological-image analysis.  
1062 *Nat. Methods.* **9**, 676-682 (2012).
- 1063 37. Ollion,J., Cochenneec,J., Loll,F., Escude,C., & Boudier,T. TANGO: a generic  
1064 tool for high-throughput 3D image analysis for studying nuclear organization.  
1065 *Bioinformatics.* **29**, 1840-1841 (2013).
- 1066 38. Preibisch,S., Saalfeld,S., Schindelin,J., & Tomancak,P. Software for bead-  
1067 based registration of selective plane illumination microscopy data. *Nat. Methods.*  
1068 **7**, 418-419 (2010).
- 1069 39. Kone,M. *et al.* LKB1 and AMPK differentially regulate pancreatic beta-cell  
1070 identity. *FASEB J.* **28**, 4972-4985 (2014).
- 1071 40. Thorens,B. *et al.* Ins1 knock-in mice for beta cell-specific gene recombination.  
1072 *Diabetologia* **58**, 558-656 (2015).
- 1073 41. Luo,J. *et al.* A protocol for rapid generation of recombinant adenoviruses  
1074 using the AdEasy system. *Nat. Protoc.* **2**, 1236-1247 (2007).
- 1075 42. Ravier,M.A. & Rutter,G.A. Isolation and culture of mouse pancreatic islets for  
1076 ex vivo imaging studies with trappable or recombinant fluorescent probes.  
1077 *Methods Mol. Biol.* **633**, 171-184 (2010).
- 1078 43. Janjuha,S. *et al.* Age-related islet inflammation marks the proliferative decline  
1079 of pancreatic beta-cells in zebrafish. *Elife.* **7.**, 32965 (2018).
- 1080 44. Zheng,G.X. *et al.* Massively parallel digital transcriptional profiling of single  
1081 cells. *Nat. Commun.* **8**:14049 (2017).
- 1082 45. Baron,M. *et al.* A Single-Cell Transcriptomic Map of the Human and Mouse  
1083 Pancreas Reveals Inter- and Intra-cell Population Structure. *Cell Syst.* **3**, 346-360  
1084 (2016).
- 1085 46. Butler,A., Hoffman,P., Smibert,P., Papalexi,E., & Satija,R. Integrating single-  
1086 cell transcriptomic data across different conditions, technologies, and species.  
1087 *Nat. Biotechnol.* **36**, 411-420 (2018).

- 1088 47. Mi,H. *et al.* PANTHER version 11: expanded annotation data from Gene  
1089 Ontology and Reactome pathways, and data analysis tool enhancements.  
1090 *Nucleic Acids Res.* **45**, D183-D189 (2017).
- 1091 48. Gut,P. *et al.* Whole-organism screening for gluconeogenesis identifies  
1092 activators of fasting metabolism. *Nat. Chem. Biol.* **9**, 97-104 (2013).
- 1093 49. Markovic,R. *et al.* Progressive glucose stimulation of islet beta cells reveals a  
1094 transition from segregated to integrated modular functional connectivity patterns.  
1095 *Sci. Rep.* **5**, 7845 (2015).
- 1096 50. Diraison,F. *et al.* Over-expression of sterol-regulatory-element-binding  
1097 protein-1c (SREBP1c) in rat pancreatic islets induces lipogenesis and decreases  
1098 glucose-stimulated insulin release: modulation by 5-aminoimidazole-4-  
1099 carboxamide ribonucleoside (AICAR). *Biochem. J.* **378**, 769-778 (2004).
- 1100 51. Rodriguez-Diaz,R. *et al.* Noninvasive in vivo model demonstrating the effects  
1101 of autonomic innervation on pancreatic islet function. *Proc. Natl. Acad. Sci. U. S.*  
1102 *A.* **109**, 21456-21461 (2012).
- 1103 52. Ilegems,E. *et al.* Light scattering as an intrinsic indicator for pancreatic islet  
1104 cell mass and secretion. *Sci. Rep.* **5**, 10740 (2015).
- 1105 53. Nyqvist,D. *et al.* Donor islet endothelial cells in pancreatic islet  
1106 revascularization. *Diabetes.* **60**, 2571-2577 (2011).
- 1107 54. Westacott,M.J., Ludin,N.W.F., & Benninger,R.K.P. Spatially Organized beta-  
1108 Cell Subpopulations Control Electrical Dynamics across Islets of Langerhans.  
1109 *Biophys. J.* **113**, 1093-1108 (2017).
- 1110 55. Reinbothe,T.M., Safi,F., Axelsson,A.S., Mollet,I.G., & Rosengren,A.H.  
1111 Optogenetic control of insulin secretion in intact pancreatic islets with beta-cell-  
1112 specific expression of Channelrhodopsin-2. *Islets.* **6**, e28095 (2014).
- 1113 56. Lorincz,R. *et al.* In vivo monitoring of intracellular Ca(2+) dynamics in the  
1114 pancreatic beta-cells of zebrafish embryos. *Islets.* **10**, 221-238 (2018).
- 1115 57. Gosak,M. *et al.* Critical and Supercritical Spatiotemporal Calcium Dynamics in  
1116 Beta Cells. *Front Physiol.* **8**, 1106 (2017).
- 1117 58. Ammala,C., Ashcroft,F.M., & Rorsman,P. Calcium-independent potentiation  
1118 of insulin release by cyclic AMP in single beta-cells. *Nature.* **363**, 356-358 (1993).
- 1119 59. Lu,T.T. *et al.* The Polycomb-Dependent Epigenome Controls beta Cell  
1120 Dysfunction, Dedifferentiation, and Diabetes. *Cell Metab.* **27**, 1294-1308 (2018).  
1121  
1122  
1123  
1124

1125 **Figure legends**

1126 **Figure 1. Glucose-stimulated  $\text{Ca}^{2+}$  influx imaged *in vivo* in the living zebrafish.**

1127 **a.** Cartoon representing a transgenic zebrafish larva expressing the genetically-encoded  
1128  $\text{Ca}^{2+}$  indicator GCaMP6s (green) and the nuclear marker cdt1-mCherry (red) under the  
1129 insulin promoter. GCaMP6s allows the examination of glucose-induced  $\text{Ca}^{2+}$ -influx in the  $\beta$   
1130 cell reported by changes in the green fluorescence in a  $\text{Ca}^{2+}$  concentration-dependent  
1131 fashion. **b.** Maximum intensity projections of an islet imaged before, during and after the  
1132 intra-cardiac injection of 5 nL of 25 mM glucose solution. Imaging and glucose stimulation  
1133 were performed simultaneously. Note the near-synchronous increase in GCaMP6  
1134 fluorescence intensity across all the  $\beta$  cells in the islet upon glucose injection. **c.** A trace  
1135 showing cumulative normalized fluorescent intensity over time for the cells shown in A. The  
1136 black arrow marks the instance of the glucose injection. **c'.** Normalized fluorescence  
1137 intensity over time for each individual cell. Each cell is represented by a square. The  
1138 normalized GCaMP6 fluorescence is displayed as a heat-map, showing the degree of cell  
1139 activity ( $n=10$  animals, not graphically represented here). **d.** Quantification of the islet  
1140 response to glucose stimulation. The graph depicts the GCaMP6 area under the curve  
1141 covering 100 seconds before and 100 seconds after the glucose stimulation ( $n=3$ , paired two  
1142 tail t-test,  $P=0.0108$ , data are means  $\pm$  SD). The injection of glucose led to a dramatic  
1143 increase in GCaMP6 fluorescence intensity. **e.** Changes in measured free glucose  
1144 concentration in larvae following glucose injection as in A. Each dot represents a pool of 10  
1145 injected larvae. ( $n=3$  for each time point, one-tailed ANOVA, with Tukey's multiple  
1146 comparisons test,  $P=0.0488$  for 0 vs. 5min and  $P=0.0152$  for 5 vs.15min). Data are means  
1147  $\pm$  SD. Scale bars, 10  $\mu\text{m}$ . The cartoons shown in panel (a) belong to the authors of this  
1148 study. The experiments in **b,c** were performed three independent times with several samples  
1149 showing similar results. **d** shows a quantification from three biological replicates from one of  
1150 the repeats. The experiment in **e** was performed once with multiple samples.

1151

1152

1153 **Figure 2.  $\text{Ca}^{2+}$  dynamics and connectivity in zebrafish: slow imaging acquisition (frame**  
1154 **rate 0.1Hz).**

1155 **a.** Single confocal planes acquired during each time window (labelled i-v) show an increase  
1156 in GCaMP fluorescence intensity during time window iii (i.e. coinciding with intracardiac  
1157 glucose injection) but no strong GCaMP signal before glucose injection (time windows i-ii)  
1158 or after glucose injection (time windows iv-v). Time windows i-v were 100 s long. **b.**  
1159 Representation of a normalised fluorescence trace generated by each  $\beta$ -cell region of

1160 interest (ROI) across the entire imaging session (1,200 s). Time windows (100s) labelled i-v  
1161 are shown at the top and the dashed line represents the time of intra-cardiac glucose  
1162 injection.  $T_{20}$  was defined as the time taken between glucose injection and the calcium  
1163 intensity spike to reach 20% above baseline. This value is tabulated for each ROI, thereby  
1164 identifying cell 2 and cell 6 as “leaders”. **c.** Cartesian functional connectivity maps displaying  
1165 the x-y position of analysed cells (numbered black dots). Cells are connected with a  
1166 coloured line if the p statistic for the Pearson coefficient was < 0.001 post bootstrapping.  
1167 The strength of the cell pair correlation (the Pearson R statistic) was colour coded: red for R  
1168 of 0.75 to 1.0, yellow for R of 0.5 to 0.75 and green for R of 0.25-0.5. Results confirm an  
1169 increase in cell-cell connectivity (strength AND number) during glucose injection (time  
1170 window iii). **d.** Heat maps show the Pearson coefficient of each cell pair in a colour-coded  
1171 manner (negative correlation; dark brown (-1), no correlation; mid brown (0), high correlation;  
1172 yellow/white (1)). **e.** During time window iii (ie at time of glucose injection) the mean positive  
1173 Pearson coefficient for connected cell pairs is 0.75 +/- 4.08 (SEM), significantly higher than  
1174 before or after glucose injection (window i R 43.8 +/-1.46, ii R 0.48 +/- 2.59, iv R 46.4 +/- 5.3  
1175 and v R 0.35 +/- 3.45) (P<0.001 on one way ANOVA with Tukey’s multiple comparison). **f.**  
1176 The overall percentage of connected cell pairs is elevated (46% +/- 6.18% SEM) during the  
1177 glucose injection compared to the rest time points (window i 15.3% +/- 2.4, window ii 10% +/-  
1178 1.86, iv 18.6% +/- 4.6 and window v 11.1% +/- 2.7). (n=6, P<0.001 one way ANOVA with  
1179 Tukey’s).

1180  
1181

1182 **Figure 3.  $Ca^{2+}$  dynamics and connectivity examined in zebrafish during rapid image**  
1183 **acquisition.**

1184 **a.** Example islet single confocal slices acquired at 3 frames/s before and during glucose  
1185 injection. Associated Cartesian connectivity maps and Pearson heatmaps (as described in  
1186 detail in Figure 2) are given below. **b.**  $Ca^{2+}$  traces from individual ROIs in the imaged islet.  
1187 The dashed line represents the time of intracardiac glucose injection. As described in Figure  
1188 2, the time to 20% rise in  $Ca^{2+}$  signal post glucose injection was measured, and tabulated in  
1189 order to identify the first responders or “temporal leaders”. **c.** Pooled data for the five  
1190 animals imaged. The mean Pearson coefficient of correlation rose significantly from the low  
1191 to high glucose state (n=5, data are means  $\pm$  SEM, p<0.001 on paired two-tailed t-test). **d.**  
1192 The percentage of significantly connected cell pairs also increases significantly following  
1193 glucose administration. Data are means $\pm$ SEM and \*\*p<0.01 following a paired two-tailed t-  
1194 test). **e.** 3D islet projections acquired at 0.8 Hz before and during glucose injection. **f.**  
1195 Associated 3D map showing the time of response in a colour-key fashion (red colour

1196 represents the fastest response). **g.** Cartesian connectivity map and Pearson heatmaps for  
1197 the islet shown in e ( $n=3$  animals, not graphically represented here). The experiment in **e,f,g**  
1198 was performed once with three samples showing similar results.

1199

1200

1201 **Figure 4. Ablation of temporally-defined “leader” cells (but not follower cells) alters**  
1202 **islet responsivity to glucose *in vivo* in the zebrafish.**

1203 **a-b.** Images from the time-lapse recording (six frames/second, single plane) of the islet  
1204 following three consecutive glucose stimulations before and after “leader” or “follower”  
1205 (control) cell ablation. Glucose was injected at 5 min. intervals whilst  $Ca^{2+}$  dynamics were  
1206 monitored. After the identification of presumptive “follower” or “leader” cells, these cells were  
1207 ablated using a two-photon laser ablation (see Methods). An X. indicates the targeted cells.  
1208 The top panels show representative frames from the movies before and after the ablation of  
1209 a “follower” (a) or a “leader” cell (b). The lower traces (a'-b') show the normalized GCaMP6  
1210 fluorescence traces and the peak in  $Ca^{2+}$  influx following glucose injection pre- and post-  
1211 ablation. **c.** Quantification of the Area Under the Curve (A.U.C.) reflecting 200 frames of  
1212 normalized GCaMP6 fluorescence before and after the ablation of a “follower” or a “leader”  
1213 cell ( $n = 20$  islets each) (paired two-tailed t-test,  $P= 3.43 \times 10^{-5}$ , ns: not significant). The  
1214 ablation of “leader”, but not “follower” cells, led to a significant reduction in the total islet  
1215 GCaMP response. Each data-point represents the mean A.U.C from three glucose-  
1216 injections in individual larvae. Data are means  $\pm$  SD. The experiments were performed eight  
1217 independent times with several samples showing similar results.

1218

1219 **Figure 5.  $Ca^{2+}$  waves and connectivity revealed using islets expressing GCaMP6f**  
1220 **throughout the cell population under insulin promoter control.**

1221 **a.** (i) Image of a donor islet that implanted onto the iris of a syngeneic recipient. Islets  
1222 indicated with arrows. (ii) Individual cells identified within a single islet were analysed. **b.**  
1223 Imaging for 10 minutes at 1fps of an islet that was exposed to chronically elevated circulating  
1224 glucose levels (measured values indicated at the time points they were measured along the  
1225 top).  $Ca^{2+}$  traces from 50 individual  $\beta$  cell ROIs are superimposed, demonstrating retained  
1226 coordination of wave behaviour over time **c.** Pearson heat maps and Cartesian connectivity  
1227 maps in two dimensions (2D – upper four panels) and 3D (lower four panels). The sharp  
1228 increase in  $\beta$  cell connectivity occurs in 3D across the entire islet and mirrors what is  
1229 captured in 2D (single plane). **d** and **e.** Pooled data for the three animals imaged in 3D.  
1230 Note that the rise in mean Pearson coefficient of  $\beta$  cell connectivity and proportion (%) of  
1231 cells connected in the low *versus* high glucose state in 3D was comparable to that measured

1232 in 2D. 2D image dataset ( $n=5$  islets in 5 different animals, not graphically represented here)  
1233 revealed a mean rise in Pearson R from  $46.4 \pm 7.2$  to  $92.6 \pm 0.9$  ( $P < 0.01$  on two-tailed t-  
1234 test) and rise in % connectivity from  $19.7 \pm 5.5\%$  to  $88.8 \pm 5.9\%$  ( $P < 0.001$  on two-tailed  
1235 t-test).

1236

1237

1238 **Figure 6. Binarized and Granger causality analysis corroborates the existence of**  
1239 **super-connected leader cells in mouse islets *in vivo*.** **a.** Pooled data for average R and  
1240 % connectivity measurements in mouse islets ( $n=5$  in 5 different animals, individual  
1241 datapoints shown) imaged over 60 minutes, with prolonged ( $>10$  minute) exposure to high  
1242 circulating glucose levels. Connectivity was recorded in the high glucose state ( $>10$  mM),  
1243 medium (6-10mM) and low ( $<4$  mM) state from the same  $\beta$  cell ROIs. Prolonged exposure  
1244 to high glucose levels does not abrogate the connectivity readout or result in dysynchrony. **b.**  
1245 Topographic representation of connected  $\beta$  cells as extracted using the binarized and Monte  
1246 Carlo data analysis approach for the same islet shown in Figure 5. Topographical  
1247 representation of  $\beta$  cell connections in the remaining four islets imaged are shown in **b'**. The  
1248 top 20-40% connected cells (reminiscent of previously-defined *in vitro* hubs) are highlighted  
1249 in white. **c.** Log-log graph of the distribution of cell-cell connections pooled across all five  
1250 islets imaged reveals a scale-free network (obeying a power-law distribution) whereby 8%  
1251 cells serve the majority (60-100%) connections. **d.** Section of fluorescence intensity  
1252 readouts for all 26 cells identified during a typical  $\text{Ca}^{2+}$  wave (superimposed in different  
1253 colours) in a single islet. Data collected at 1.0 frame per second, the calcium waves shown  
1254 here occurred in the high glucose state (25 mM). **e.** Close up of the fluorescent profiles for  
1255 each individual cell taking part in the islet  $\text{Ca}^{2+}$  wave. "Leader cells" can be defined  
1256 temporally as preceding the activity of "follower" cells. **f.** Yellow markers highlight the  
1257 position of the temporally-defined "leaders". Results are shown in Supplementary Table 1  
1258 (Animal #1). Note that temporally the four defined "leaders" are always the most connected  
1259 on independent Granger Causality analysis.

1260

1261

1262

1263

1264

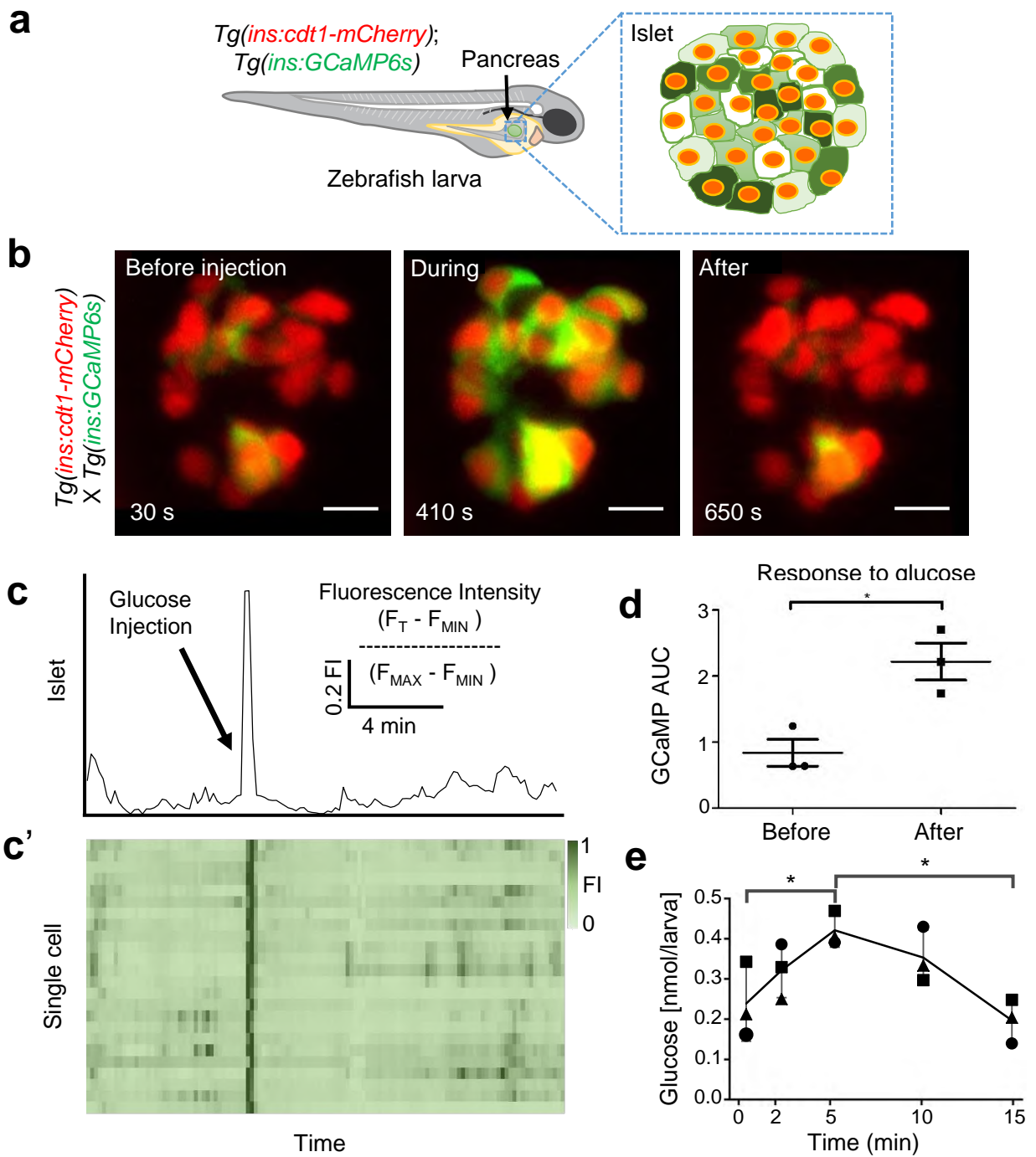


Figure 1



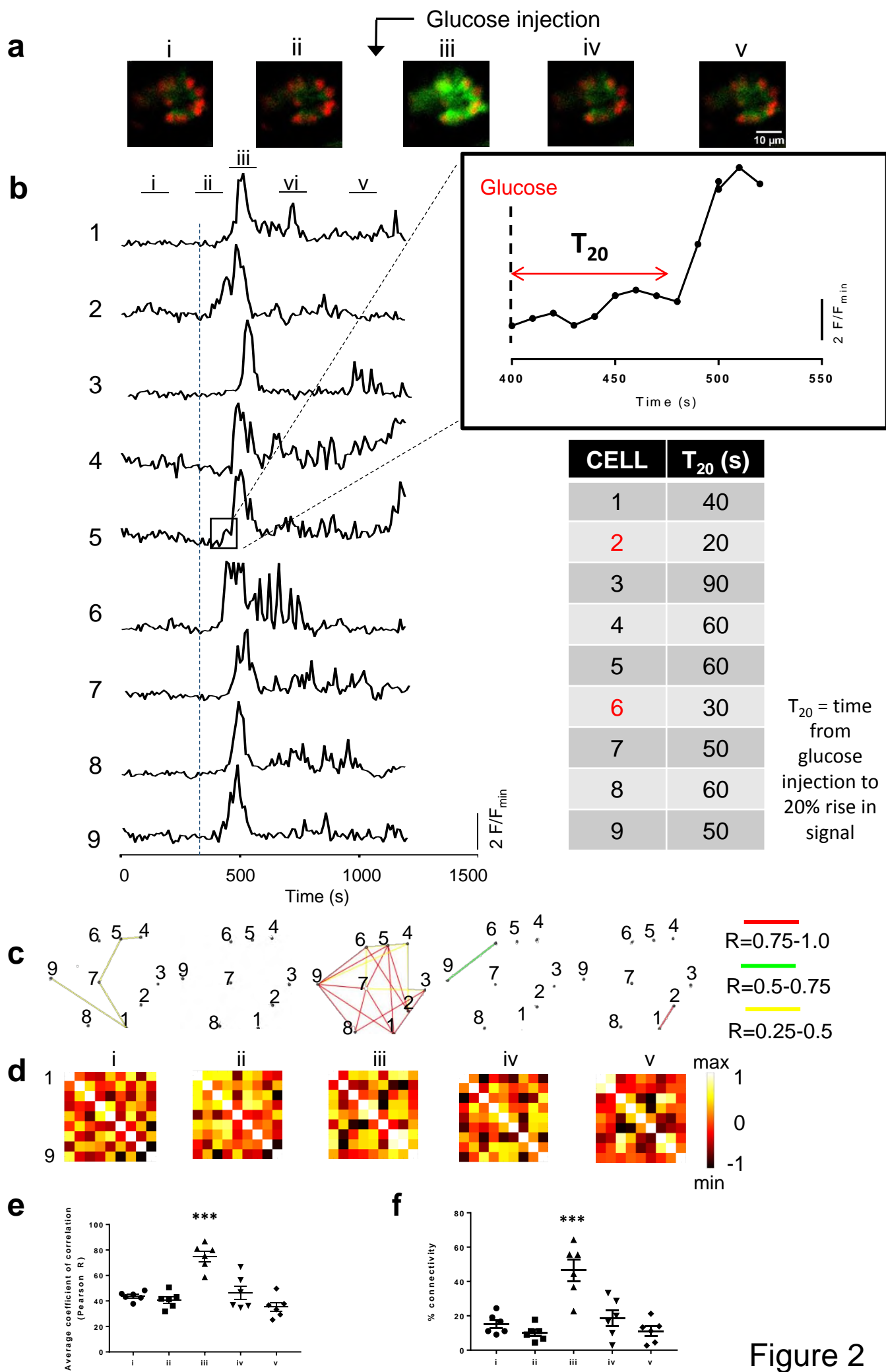


Figure 2

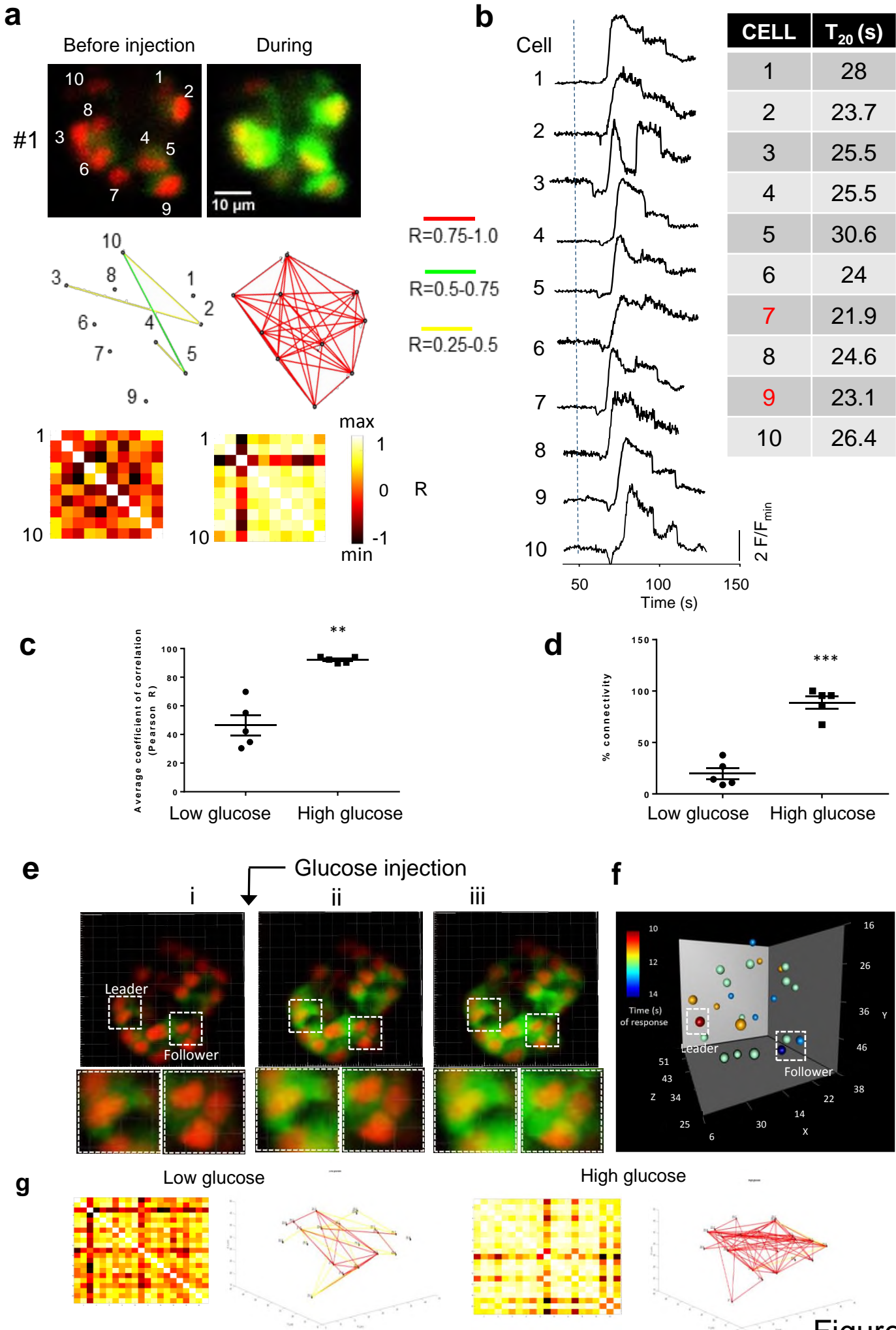


Figure 3

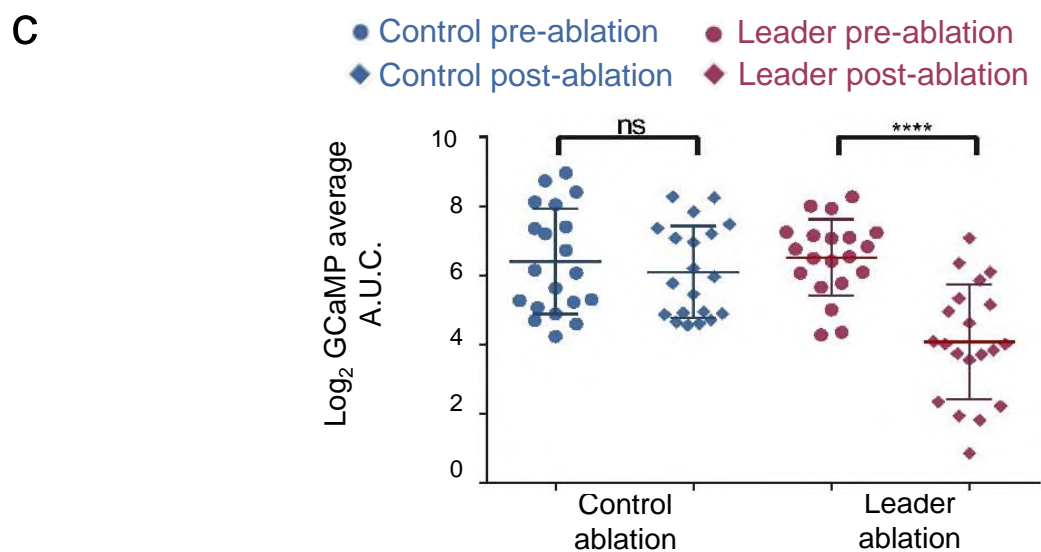
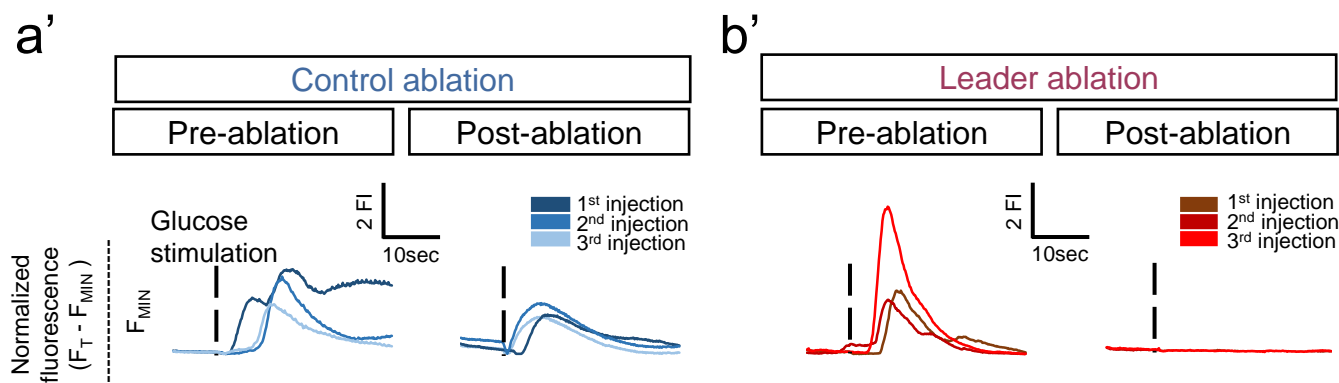
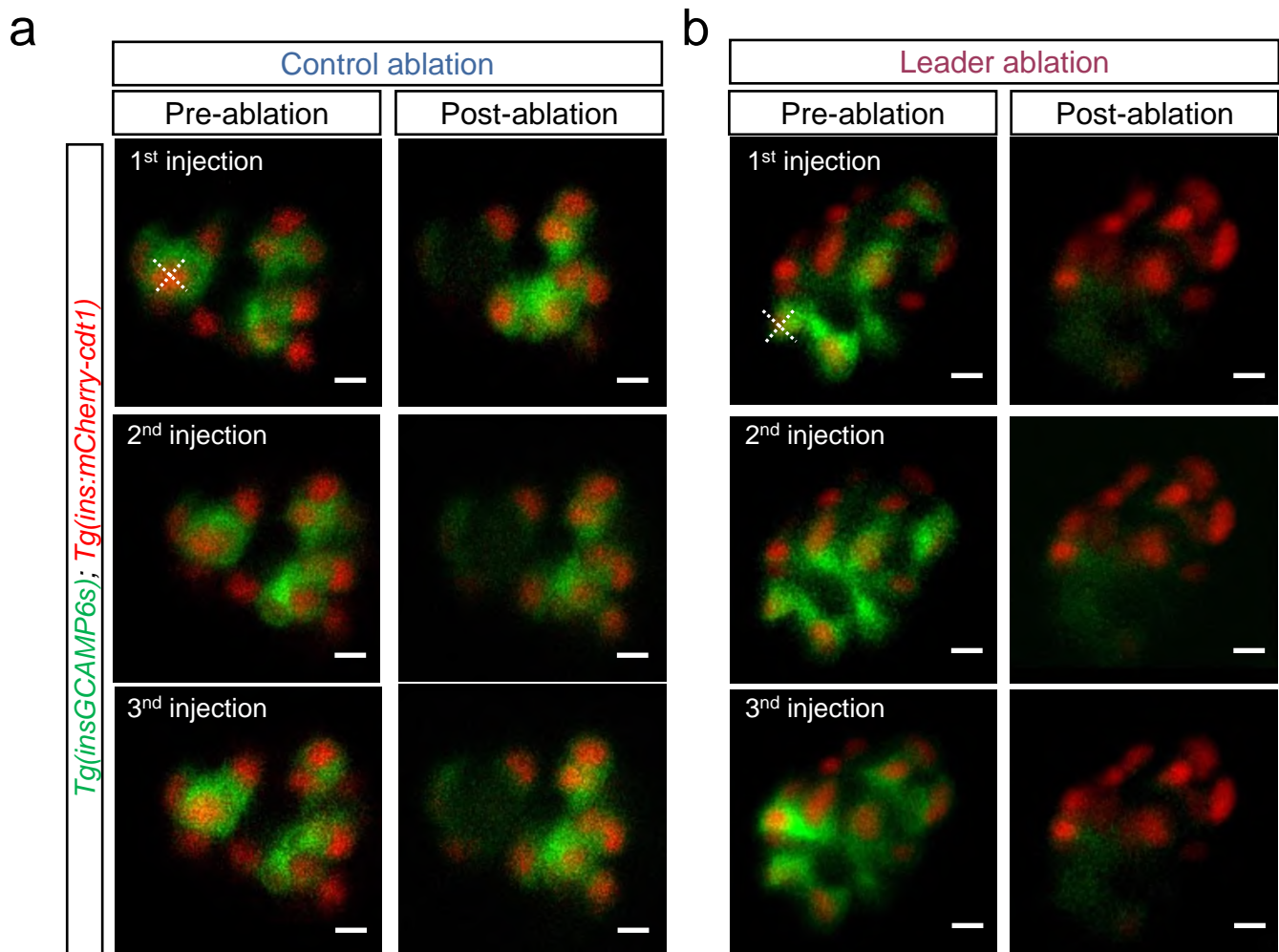


Figure 4

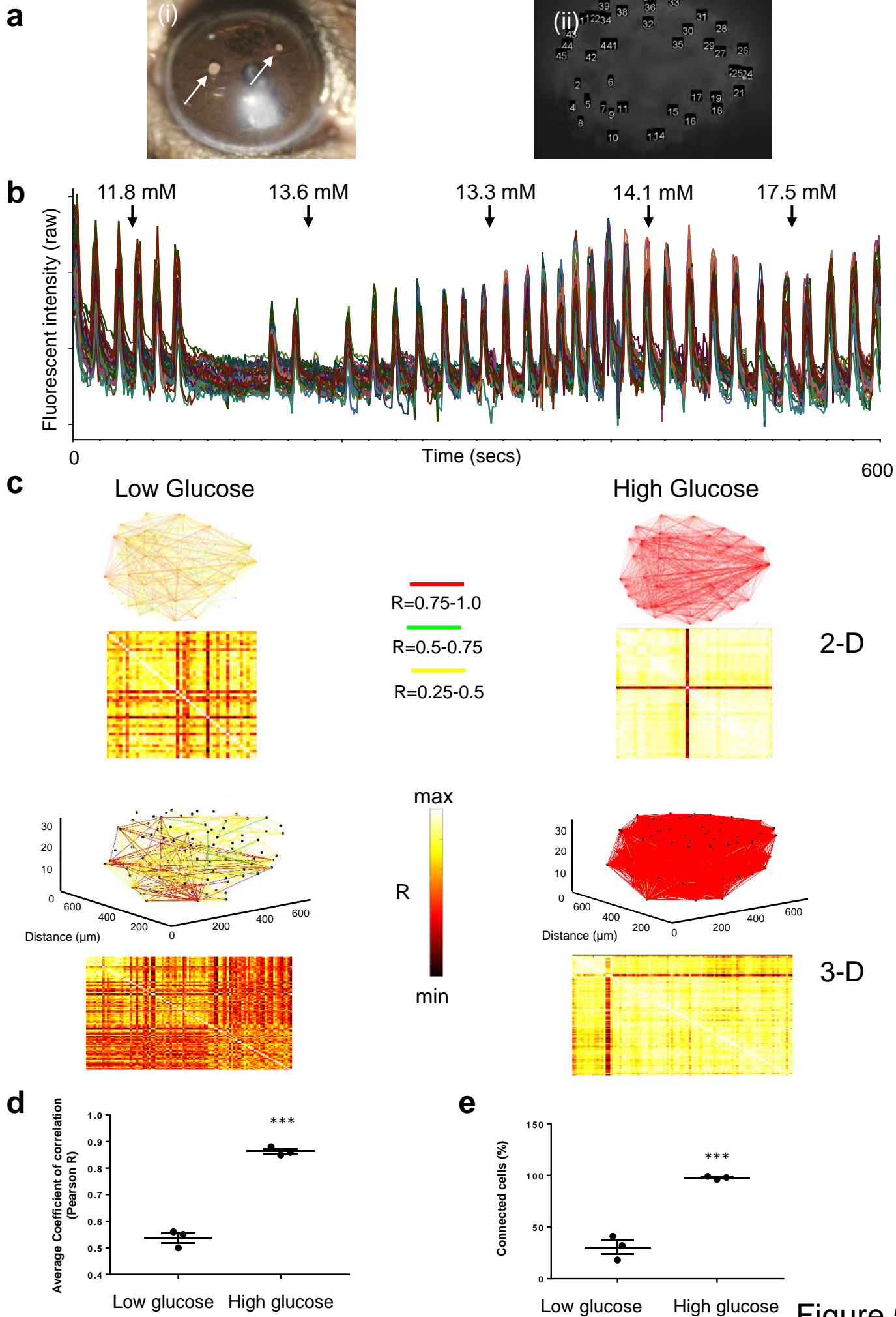


Figure 5

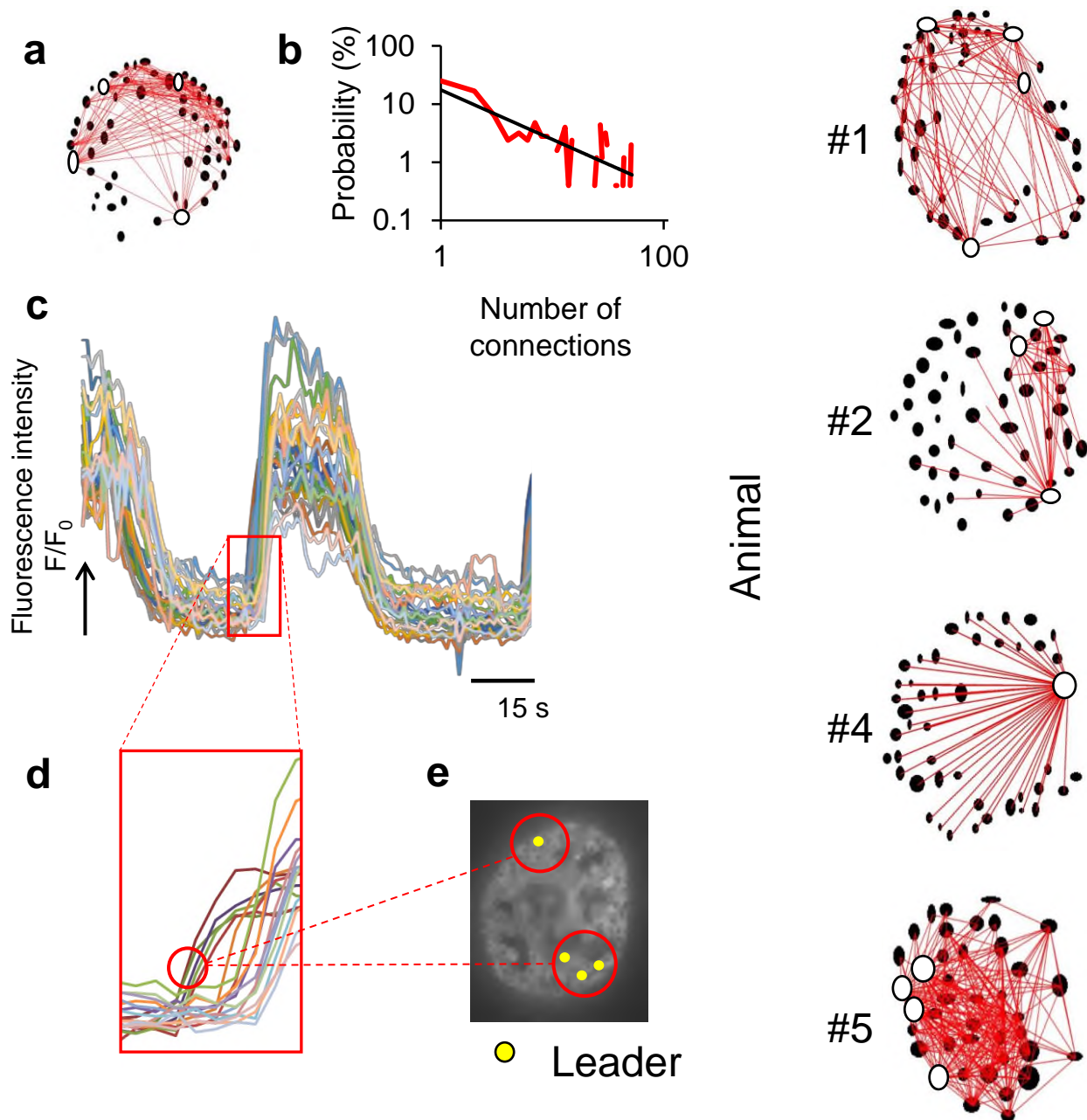
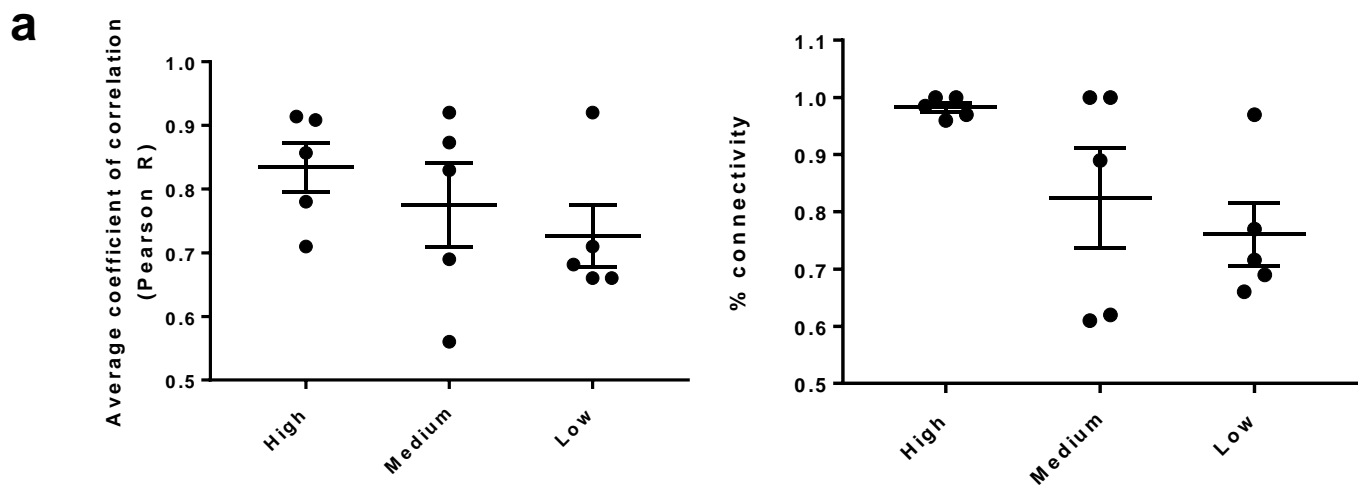


Figure 6

# Leader $\beta$ cells coordinate calcium dynamics across pancreatic islets in vivo

NATMETAB-A18060205A

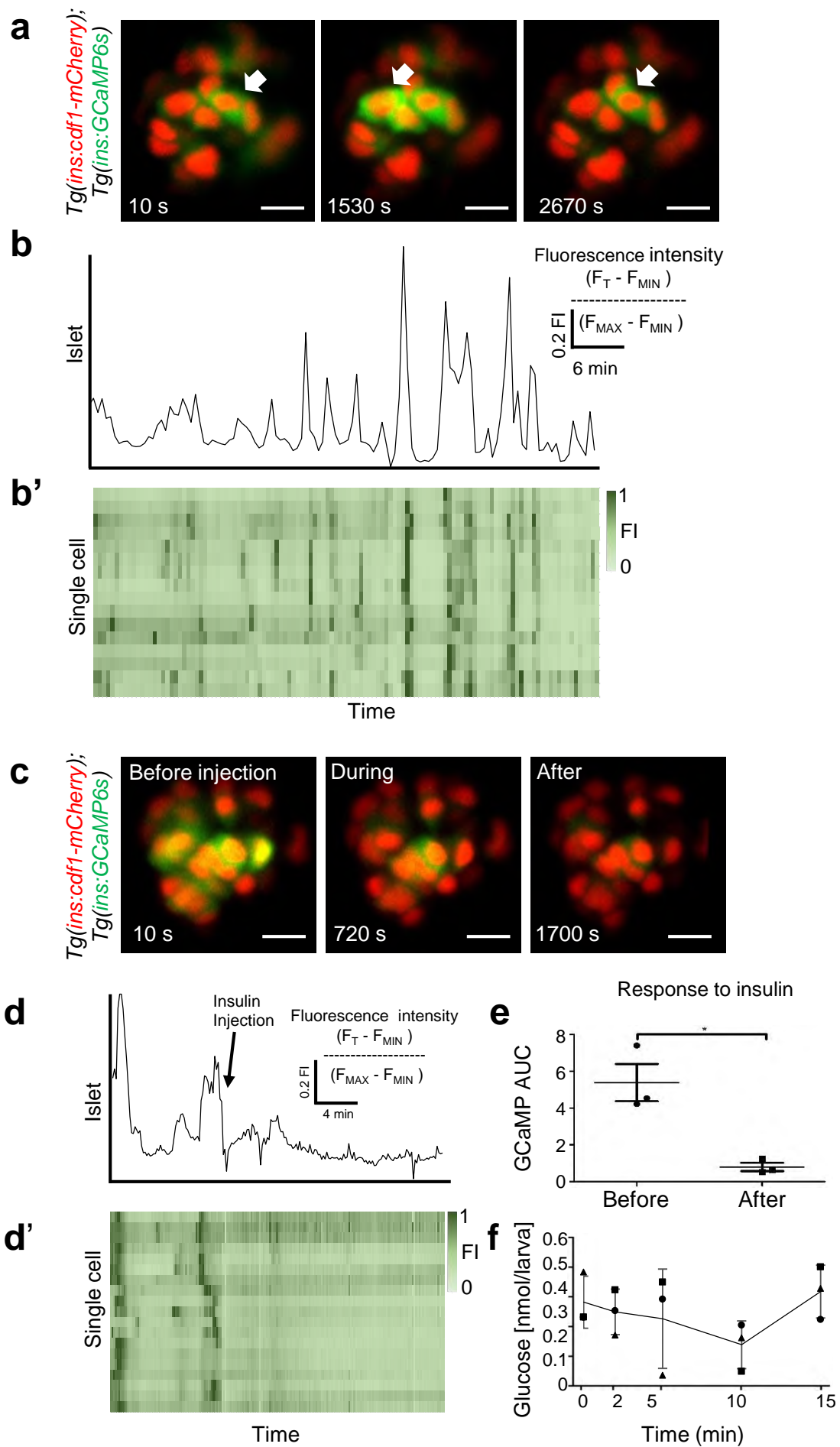
## Supplementary Information

**Supplementary Table 1.  $\text{Ca}^{2+}$  dynamics and connectivity in zebrafish: fast imaging acquisition (frame rate 1 to 3 Hz).**  $T_{20}$  values, defined as the time taken (s) between glucose injection and the  $\text{Ca}^{2+}$  intensity spike to reach 20% above baseline for each ROI (cell), are shown. Values corresponding to temporally-defined “leader” cell(s) for a given animal are highlighted in red. See also Figure 5.

Cell/Animal	# 1	# 2	# 3	# 4	# 5
1	28	34.2	48.3	20.7	18.6
2	23.7	32.7	45.6	24.3	19.5
3	25.5	37.5	48	26.1	19.5
4	25.5	41.1	43.5	33.6	19.2
5	30.6	38.1	48.6	32.1	19.8
6	24	37.2	48.3	31.5	21
7	21.9	27	49.5	21.3	19.5
8	24.6	38.4	51	21.3	19.8
9	23.1		47.7	21.3	21.6
10	26.4		47.7	20.4	20.1
11				24.9	

**Supplementary Table 2:** Granger connection results for the top four temporally defined “leader cells” in the indicated mouse islets (GCaMP6f driven by the insulin promoter).

Mouse islet (GCaMP6 driven by insulin promoter) [Number of ROIs i.e. cells analysed]	Temporally defined leader cell (numbered 1 – 4 i.e. the first responders to high glucose)	Number of cells to which the temporally-defined leader is causally connected on independent Granger analysis
#1	1	26
	2	26
	3	26
	4	26
#2 [26]	1	26
	2	26
	3	26
	4	26
#3 [44]	1	43
	2	44
	3	44
	4	44
#4 [27]	1	14
	2	13
	3	14
	4	15
#5 [38]	1	33
	2	35
	3	36
	4	36



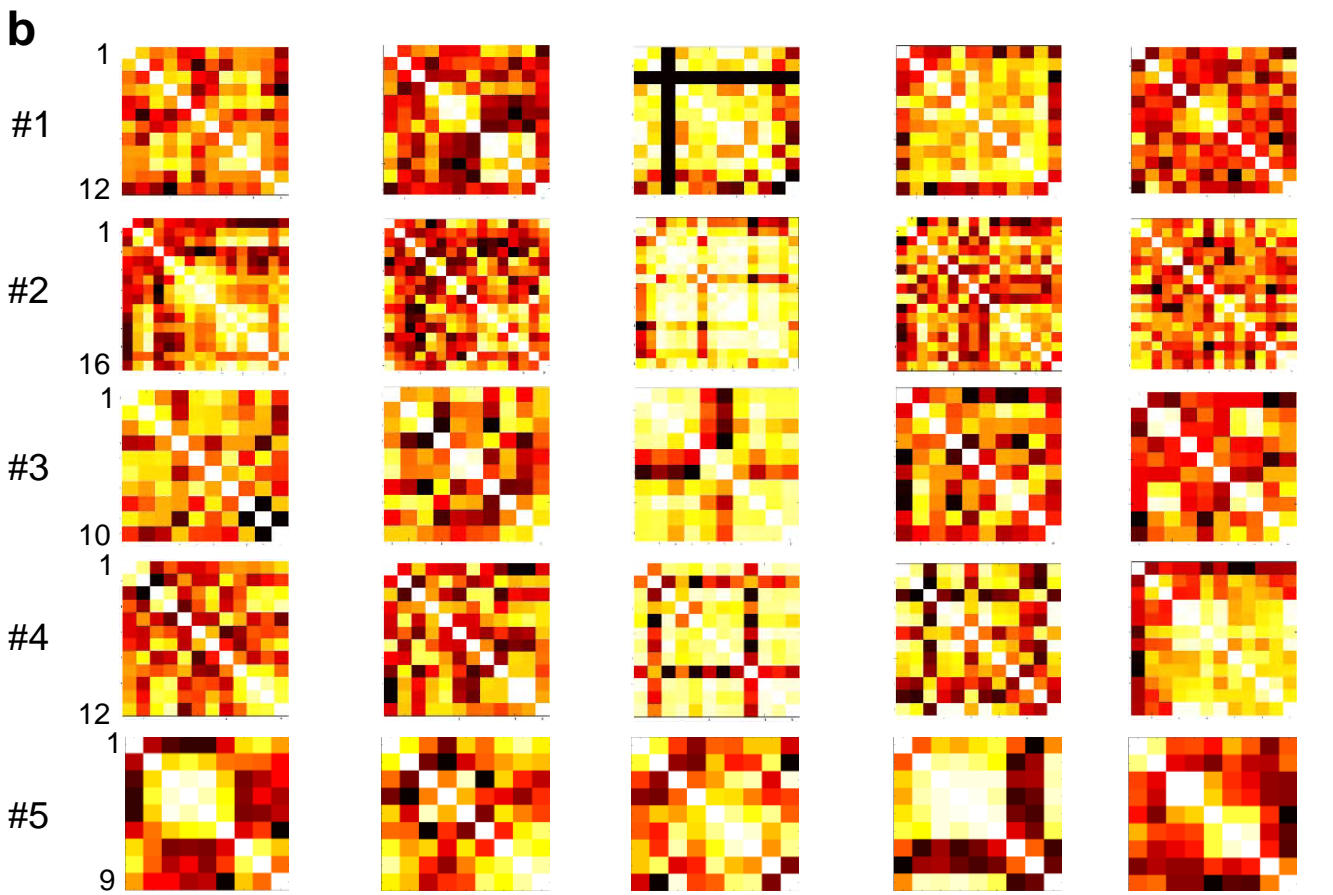
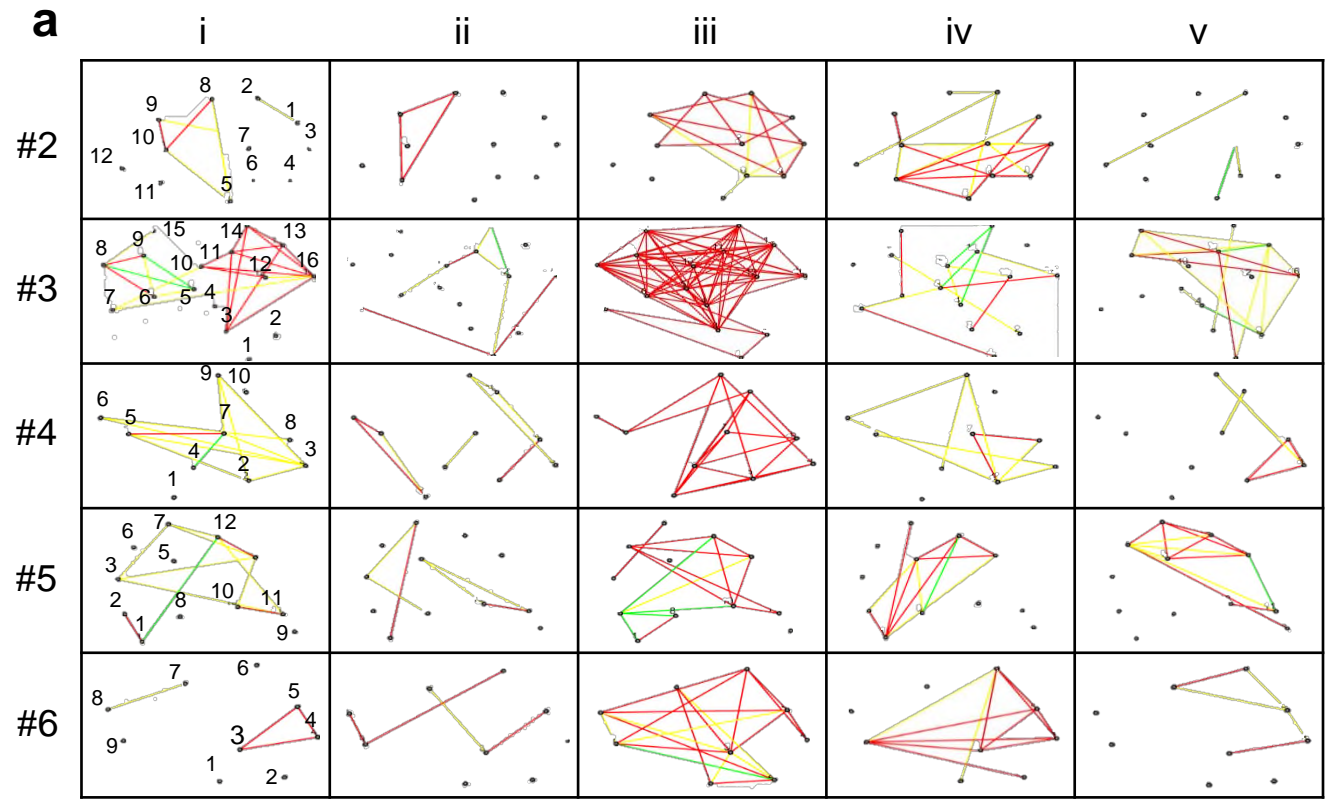
Supplementary Figure 1



Supplementary Figure 1. **Endogenous Ca<sup>2+</sup> transients imaged in vivo in the living zebrafish: spontaneous Ca<sup>2+</sup> transients are suppressed by insulin.**

**a.** Snapshots from time-lapse recordings of the primary islet from a larva mounted in agarose and imaged using a confocal microscope every 30 s. Arrows indicate cells exhibiting an increase in GCaMP6 signal at a given time. The images represent maximum intensity projections. **b.** The top panel shows the trace of cumulative normalized fluorescent intensity over time for the cells shown in **b**. **b'**. Normalized fluorescence intensity over time for each cell. Each cell is represented by a square. The normalized GCaMP6 fluorescence is displayed as a heat-map, showing the degree of cell activity in individual cells. **c.** Maximum intensity projections of an islet imaged before, during and after the intra-cardiac injection of 5nL of 100 Insulin units/ml of insulin. The imaging and insulin administration were performed simultaneously with a frame rate acquisition every 15 s. **d.** A trace of cumulative normalized fluorescent intensity over time for the cells shown in **A**. The black arrow marks the instance of insulin injection. **d'**. Normalized fluorescence intensity over time for each individual cell. ( $n=10$ , not graphically represented here) **e.** Quantification of the islet activity before and after the insulin injection. The graph depicts the GCaMP6 area under the curve covering 100 seconds before and 100 seconds after the insulin injection. The injection of insulin led to a reduction in GCAMP fluorescence intensity ( $n=3$  animals, paired two-tailed t-test,  $P= 0,0476$ ). Data are means  $\pm$  SD. **f.** Changes in measured free glucose concentration in larvae following insulin injection as in **c**. Each dot represents a pool of 10 injected larvae. . ( $n=3$  for each time point, one-tailed ANOVA (with Tukey's multiple comparisons test),  $P=0,3587$ ). Data are means  $\pm$  SD Scale bars, 10  $\mu$ m. The experiments in **a,b** were performed three independent times with several samples showing similar results. The experiments in **c,d** were performed three independent times with several samples showing similar results. **e** shows a quantification from three biological replicates from one of the repeats. The experiment in **f** was performed one time with several samples.

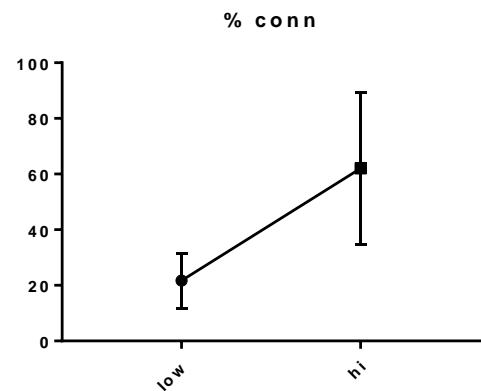
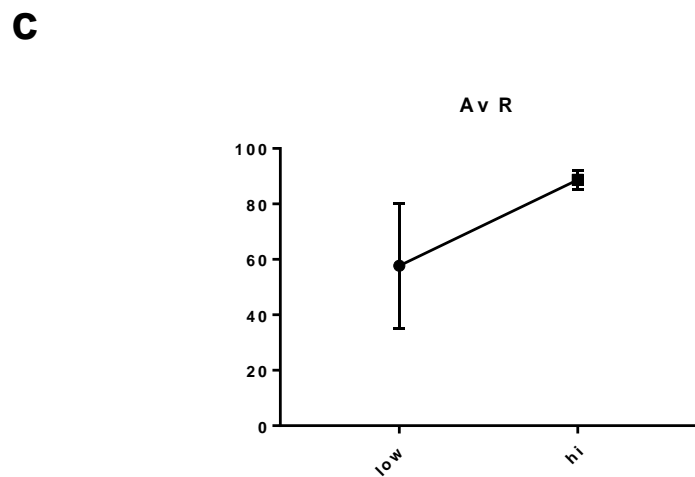
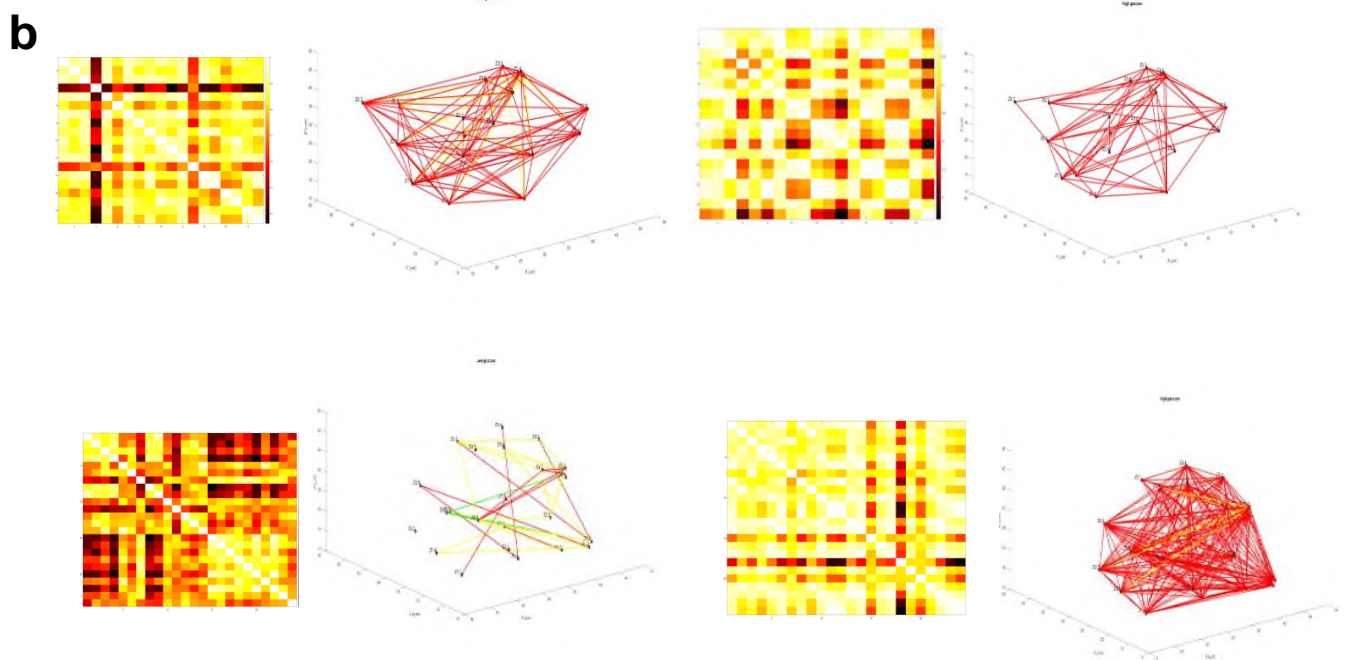
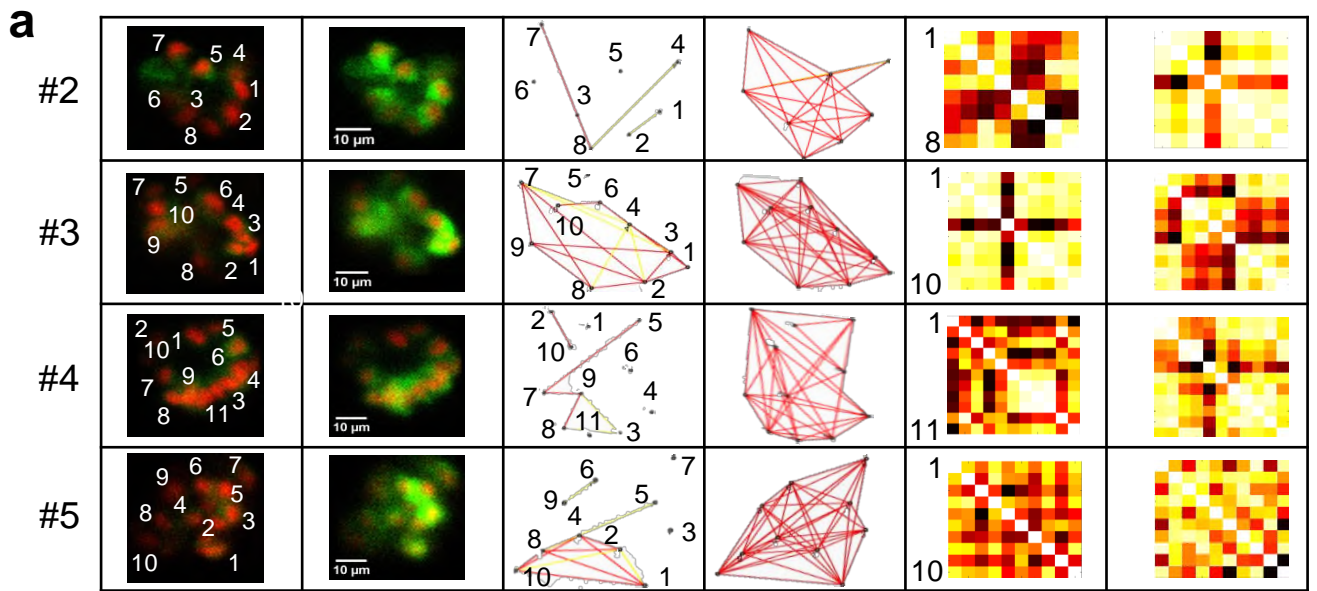
Glucose injection



Supplementary Figure 2

Supplementary Figure 2. **Ca<sup>2+</sup> dynamics and connectivity in zebrafish: slow imaging acquisition (frame rate 0.1Hz).**

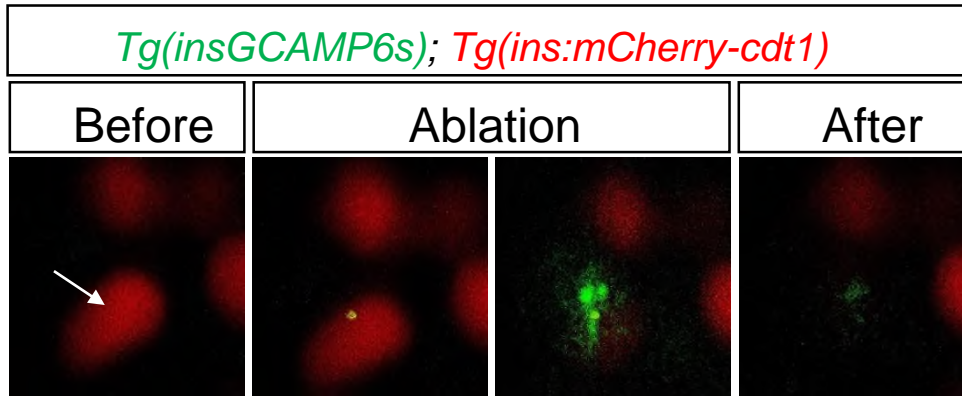
**a.** Cartesian functional connectivity maps displaying the x-y position of analysed cells (numbered black dots). Cells are connected with a coloured line if the p statistic for the Pearson coefficient was  $< 0.001$  post bootstrapping. The strength of the cell pair correlation (the Pearson R statistic) was colour coded: red for R of 0.75 to 1.0, yellow for R of 0.5 to 0.75 and green for R of 0.25-0.5. Results are shown for each of the five time windows that were analyzed (i-v, each 100 secs long) during the 1,200 second imaging period. The middle time window, iii, occurred during glucose injection. Results confirm an increase in cell-cell connectivity (strength AND number) during glucose injection (grouped in Main Figure 2 E and F). **b.** Heat maps show the Pearson coefficient of each cell pair in a colour-coded manner (negative correlation; dark brown (-1), no correlation; mid brown (0), high correlation; yellow/white (1)), across the five time windows (two before and two after glucose injection). ( $n=6$  ).



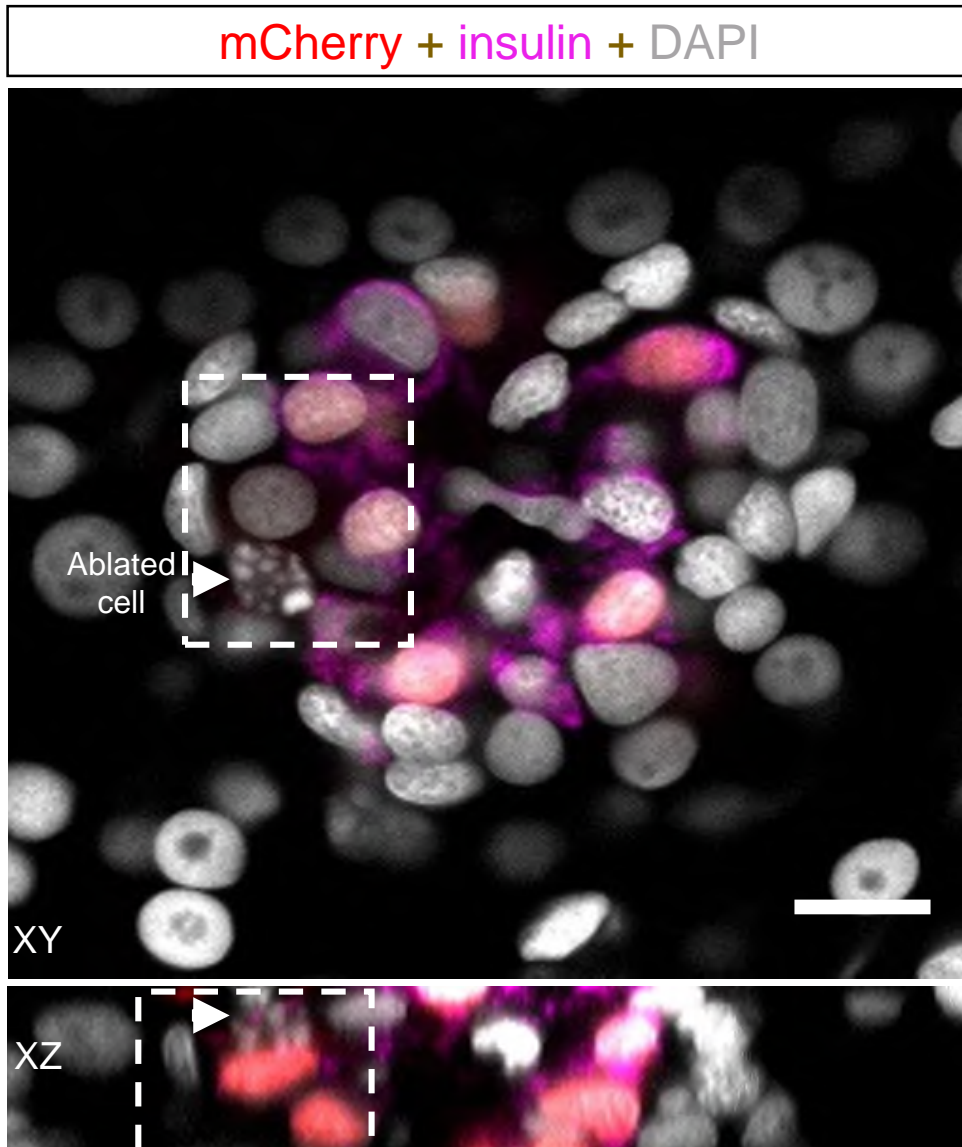
Supplementary Figure 3. **Islet connectivity in 2D and 3D.**

- a. Cartesian connectivity maps and Pearson heatmaps for the remaining animals corresponding to the 2D imaging and analysis shown in Figure 3 a-d ( $n=5$  for total experiment).
- b. Cartesian connectivity maps and Pearson heatmaps for the remaining animals corresponding to the 3D imaging and analysis shown in Figure 3 e-f ( $n=6$  for total experiment).
- c. The percentage of connected cell pairs imaged in 3D increases following glucose administration ( $n=3$ ). Data are means  $\pm$  SEM.

a



b



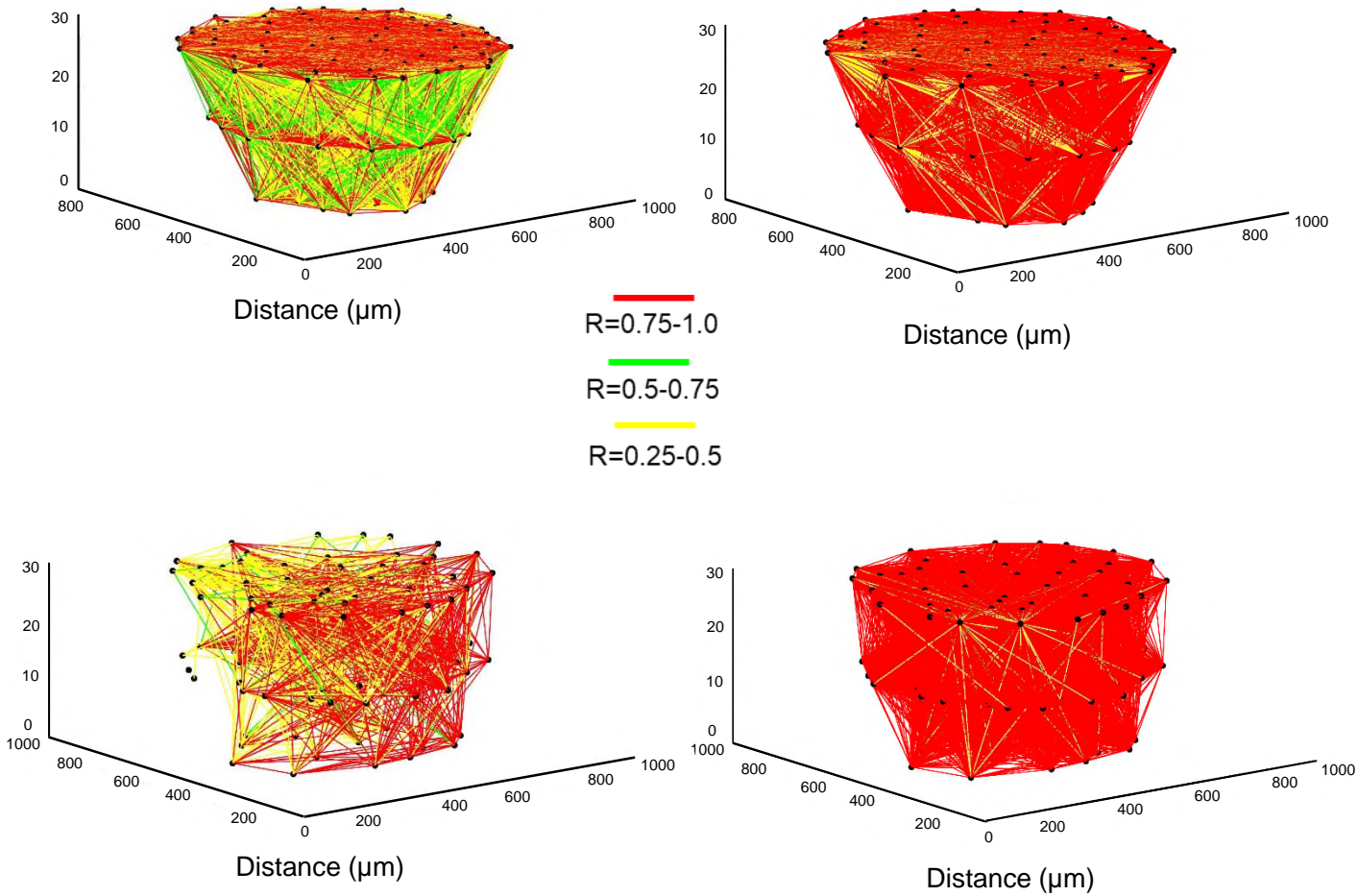
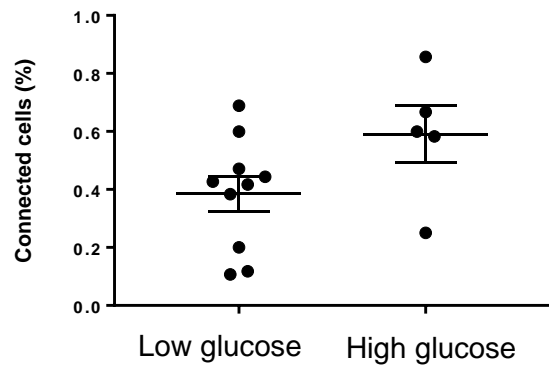
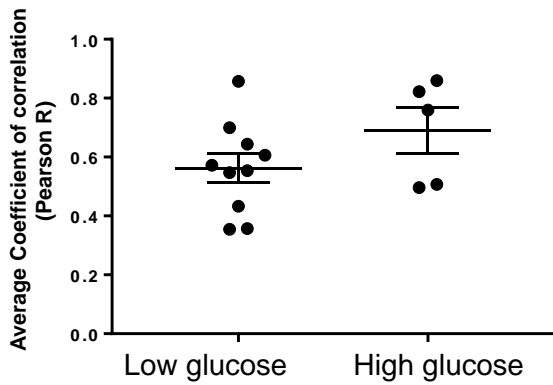
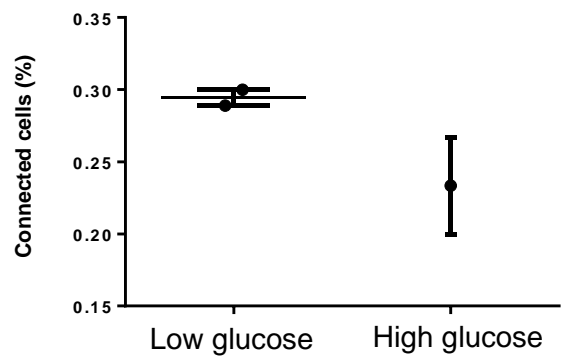
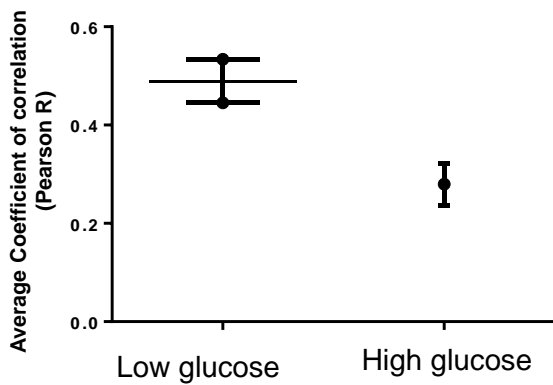
Supplementary Figure 4. **2-Photon UV ablation achieves highly targeted, single cell destruction.**

- a.** Images of a time-lapse recording in a single plane of a cell undergoing laser ablation (arrow). The snapshots show the nuclei of  $\beta$ -cells marked using *Tg(ins:mCherry-cdt1)* before, during and after the ablation of the targeted cell.
- b.** Confocal image corresponding to the islet showed in a, following fixation and immunohistochemistry against Insulin. Arrow marks the damaged nucleus of the ablated cell. The DAPI staining showed no discernible damage to neighbours cells ( $n=5$ ). Scale bar = 10 $\mu$ m. The experiment was performed on one occasion with five samples showing similar results.

**a**

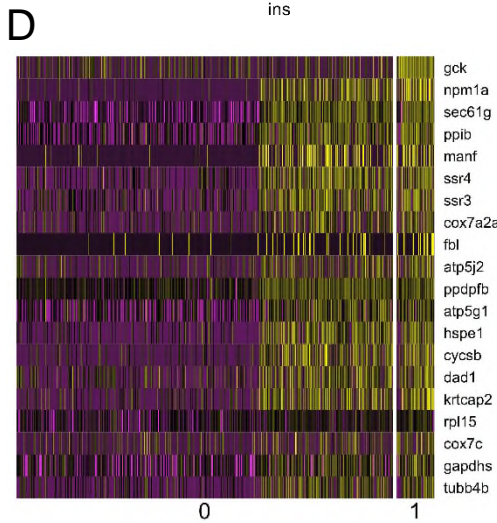
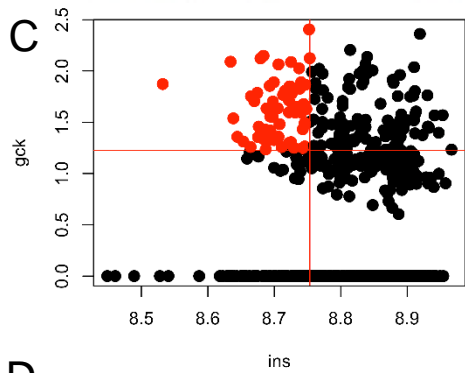
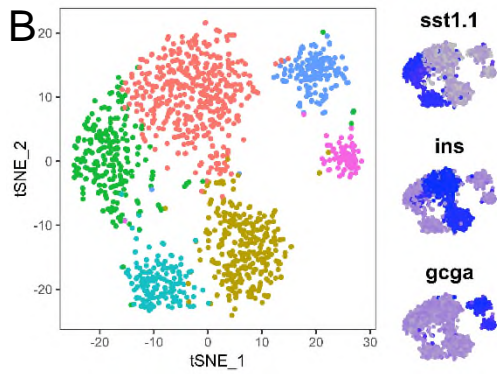
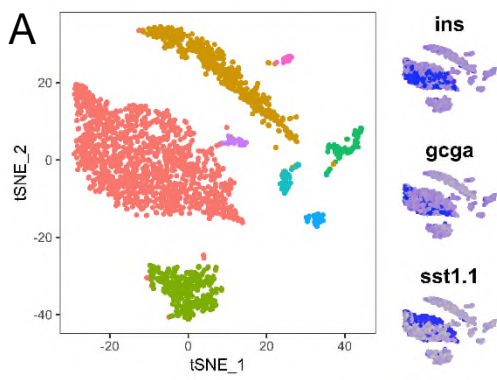
Low glucose

High glucose

**b****c**

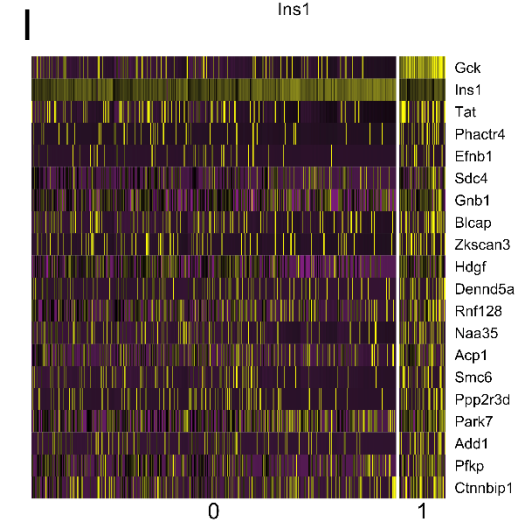
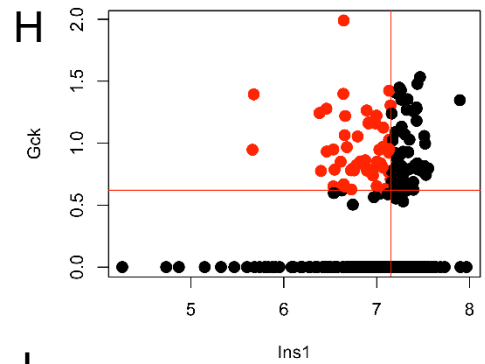
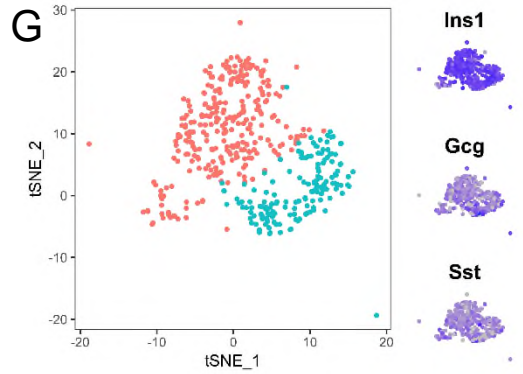
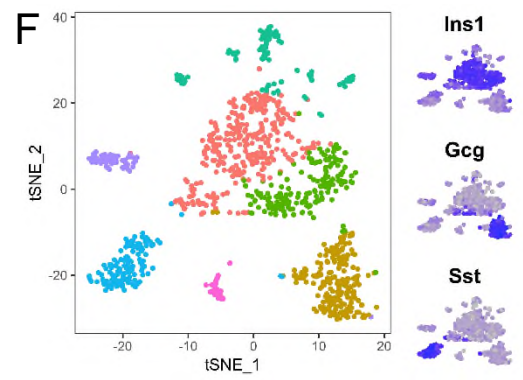


Supplementary Figure 5: **Ca<sup>2+</sup> dynamics and connectivity in mouse islets expressing GCaMP6f under the Insulin promoter.** **a.** 3D Cartesian connectivity maps and (as previously described in Supplementary Figure 2) for the remaining 2 animals not shown in Figure 5, in low *versus* high glucose states. A total of 3 islets in 3 different animals were used for this group of experiments. **b.** Pooled data for average R and % connectivity measurements in healthy human islets transplanted infected with AV-GCaMP6 and transplanted into Balb/c nu/nu recipient mice. A non-significant (on two-tailed unpaired t test) trend in increase in both indices is observed between low and high glucose levels. Healthy human islets (11 experiments) came from four individual human donors: 1. male, age at death 74, BMI 29.2; 2. male, age at death 14, BMI 21.5; 3. female, age at death 65, BMI 28.8; 4. male, age at death 50, BMI 22.9, died of cardiovascular disease. Individual data points are shown for each experiment. There are fewer data points for the “high” glucose condition because the mice did not always respond with a robust rise in glucose under the anaesthetic conditions. **c.** Two islets from a single human diabetic donor were transplanted individually. Both exhibited a reversal in trend for connectivity, which dropped from the low to high glucose state. Donor details: female, 54 years old, BMI 24.4, type 2 diabetic for 10 years, insulin dependent for the last 1.5 yrs.



**E**

GO BP	Fold Enrichment	FDR
oxidative phosphorylation	21.53	1.84E-09
respiratory electron transport chain	12.49	7.55E-09
generation of precursor metabolites and energy	9.10	5.53E-09
protein folding	8.04	5.73E-05
RNA localization	7.27	6.78E-03



**J**

GO BP	Fold Enrichment	FDR
glycolysis	17.28	1.54E-02
generation of precursor metabolites and energy	6.04	1.81E-02

Supplementary Figure 6

Supplementary Figure 6. **Single Cell RNA-Seq analysis of Zebrafish (a-e) and Mouse (f-j) islets to identify putative hub/leader cells.** **a.** t-distributed Stochastic Neighbor Embedding (TSNE) plot of initial clustering of Zebrafish islet cells shows insulin, glucagon and somatostatin-positive cells all contained in a single 'endocrine' cluster. **b.** Subsequent re-clustering of this 'endocrine' cluster separates into distinct clusters expressing insulin, glucagon and somatostatin. **c.** The pooled insulin-positive clusters were filtered to remove the few cells expressing other hormones then putative hub cells (red) were identified on the basis of higher *gck* expression and lower *ins* expression (see Results) (*n*=6 animals yielding 2625 cells). **d.** Heatmap showing the top 20 genes defining the putative hub cells. **e.** Statistically over-represented GO BP terms in genes upregulated in putative hub cells. **f.** Initial clustering of mouse islet data shows distinct clustering of cells expressing insulin, glucagon and somatostatin. **g.** The majority of insulin-positive cells were contained within the two central clusters showing little expression of the other two hormones. **h-j** The identified mouse  $\beta$  cells were analysed in a similar manner to the Zebrafish cells to identified genes defining putative hubs and overrepresented GO BP terms.